Research

Author for correspondence:
I. A. Maia
e-mail:
igor.albuquerque.maia@univ-poitiers.fr

Two-point wavepacket modelling of jet noise

I. A. Maia[1], P. Jordan[1], A. V. G. Cavalieri[2] and V. Jaunet[1]

[1]Institut PPRIME, CNRS, Université de Potiers, ENSMA, Poitiers 86036, France
[2]Divisão de Engenharia Aeronáutica, Instituto Tecnológico de Aeronáutica, São José dos Campos, Sao Paulo 122228-900, Brazil

IAM, 0000-0003-2530-0897; PJ, 0000-0001-8576-5587; AVGC, 0000-0003-4283-0232

This paper is focused on the study of a kinematic wavepacket model for jet noise based on two-point statistics. The model contains physical parameters that define its structure in terms of wavenumber, envelope shape and coherence decay. These parameters, which are necessary to estimate the sound pressure levels radiated by the source, were educed from a large-eddy simulation database of a Mach 0.4, fully turbulent jet. The sound pressure levels predicted by the model were compared with acoustic data and the results show that when the parameters are carefully educed from the data, the sound pressure levels generated are in good agreement with experimentally measured values for low Strouhal numbers and polar angles. Furthermore, here we show that a correct representation of both coherence decay and wavepacket envelope shape are key aspects to an accurate sound prediction. A Spectral Proper Orthogonal Decomposition (SPOD) of the model source was also performed motivated by the search for a low-rank model capable of capturing the acoustic efficiency of the full source. It is shown that only a few SPOD modes are necessary to recover acoustically important wavepacket traits.

1. Introduction

Jet noise is a challenging and compelling problem in fluid mechanics, because of its environmental and societal relevance but also because of disagreements that exist in the aeroacoustics community regarding its theoretical basis. Despite nearly 70 years of research, there persists a lack of consensus regarding the flow structures responsible for sound generation. The first mathematical treatment for the jet noise problem was given by Lighthill [1] by means of his acoustic analogy. The main idea of the

acoustic analogy is to rearrange the equations of motion as an inhomogeneous wave equation that separates the linear propagation of acoustic waves from a nonlinear inhomogeneous term composed of turbulent fluctuations that drive the sound field. In this framework, the turbulent field is replaced by an equivalent distribution of quadrupole sources whose statistical properties are related to those of the flow. Other acoustic analogies have since been proposed, for example, by Lilley [2] and Goldstein [3], that involve different source-propagator splits to deal with the effects of flow-acoustic interactions, but with the same central idea.

Because Lighthill's acoustic analogy is an exact rearrangement of the Navier–Stokes equation, it is possible to compute the sound field accurately if a sufficiently good description of the flow field is known. This has been strictly demonstrated for low Mach number flows and low frequencies by Crow [4]. For higher Mach number flows, it has been demonstrated by means of direct numerical simulations by Freund [5] and Colonius & Freund [6] that accurate sound predictions are also possible if the source term is calculated in the close vicinity of the jet, so as to converge the convolution between source and Green's function. However, understanding and modelling the flow entities responsible for sound generation is a daunting task, as a correct description of the source terms in acoustic analogies depends on two-point, fourth-order statistics, finely described in a volume sufficient to cover all of the source region. Given this challenge, a considerable body of work has been undertaken to characterize flow parameters important for sound radiation and to build statistical source models. The structure of the cross-correlation tensor, which is at the core of the models, has frequently been analysed by hot-wire measurements, for example, by Davies *et al.* [7], Bradshaw *et al.* [8], Davies [9], Chu [10], who focused mainly on the characterisation of length and timescales; Harper-Bourne [11,12] went further, determining the frequency-dependence of coherence and integral lengthscales at selected points in the mixing layer with a pair of hot-wires; and Morris & Zaman [13] performed a similar analysis for positions both in the mixing layer and at the centreline of the jet. Two-point measurements have also been performed using LDV by Jordan & Gervais [14] and Kerhervé *et al.* [15] for limited regions in the jet, and the frequency-dependent character of turbulence statistics has also been explored. Other studies have used PIV to probe the structure of the cross-correlation tensor in $x − r$ and $r − \theta$ planes, as done for example by Ukeiley *et al.* [16], who evaluated the structure of linear and quadratic source components separately. Similar measurements, using PIV, have been performed by Seiner *et al.* [17] and Bridges & Wernet [18]. Jaunet *et al.* [19] performed time-resolved, stereo PIV in two synchronized crossflow planes with a view to studying two-point coherence of wavepackets and comparing them to those of the energy-containing, turbulent eddies. Different components of the cross-correlation tensor have also been analysed by Karabasov *et al.* [20] using a large-eddy simulation (LES) database.

The measurements of Harper-Bourne [11,12] have been important in guiding noise-source modelling and in supporting acoustic predictions, as, for example, in the works of Self [21], Goldstein & Kharavan [22], Goldstein & Leib [23], Karabasov *et al.* [20] and Leib & Goldstein [24]. In these studies, model calculations are compared with acoustic data, and reasonable agreement is obtained for given frequency and polar-angle ranges.

While different source models are based on different descriptions of the two-point cross-correlation function, one thing they all have in common is that they require knowledge of the variation of this function with position and frequency. In previous studies the cross-correlation function was generally obtained at a small selection of positions; given this constraint, simplifying assumptions are required. For example, length and timescales are assumed to vary linearly with the ratio of kinetic energy by dissipation [22]; or the turbulence autocovariance tensor is assumed to be constant throughout the jet, with expansion coefficients assuming ad-hoc values. Moreover, again due to the lack of data, accurate sound prediction usually relies on the calibration of a number of empirical constants [21–26].

The modelling studies cited above consider sound sources based on a superposition of statistically independent, uncorrelated eddies, a view aligned with the interpretation of the acoustic analogy given by Lighthill. The parameters used in these models, such as convection velocity and length and timescales, are those of the energy-containing eddies and are obtained

from the integral length and timescales of turbulence. An alternative interpretation for the flow motions associated with sound generation came with the observation of wavepackets in turbulent jets by the experiments performed, for instance, by Mollo-Christensen [27,28] and Crow & Champagne [29]. Wavepackets are organized, low-energy structures correlated over distances that far exceed the integral length scales of turbulence. The discovery of this underlying order and its connection with sound radiation motivated researchers to explore wavepacket-like source models. We can make a distinction between two kinds of wavepacket models: dynamic and kinematic [30]. Kinematic models are built based on experimental observations or statistical properties of a flow and are usually coupled with an acoustic analogy; they are inherently empirical and mask the details of the nonlinear fluid motions by which they are underpinned. A dynamic model based on the equations of motion is necessary to obtain the underlying flow motions. Hydrodynamic stability theory has been used as a theoretical framework that would provide a dynamic law governing the evolution of wavepackets in turbulent flows. Early examples of these modelling efforts can be found in the works of Michalke [31,32], Crow & Champagne [29] and Crighton & Gaster [33]. Jordan & Colonius [34] made an extensive review of studies that have successfully used stability analysis, experiments and simulations (or a combination of these) to provide evidence for the existence of wavepackets in both the turbulent field [35–37] and the near-irrotational field [38–41]. It has also been demonstrated that the low-frequency, far-field sound is consistent with an axially extended wavepacket [31,42–44] and that it can be decomposed, almost entirely, into only three azimuthal Fourier modes [43–46].

Modelling wavepackets using linear stability theory makes it possible to capture the evolution of their power-spectral density (PSD) up to the streamwise position at which they become neutrally stable [35]. However, further downstream there is a considerable discrepancy between experiment and linear theory. For low Strouhal numbers ($St < 0.3$), the agreement is also poor. Furthermore, linear dynamic models describe harmonic solutions, so they cannot describe the two-point statistics of a turbulent flow and this may explain the lack of success of these models in predicting correct pressure levels in the far-field. Acoustic extrapolation of wavepacket solutions of the Linearized Euler Equations (LEE) leads to a 30 dB discrepancy in the far field [47]. In this spirit, a series of other papers have evoked the importance of coherence decay [41,47–50] for acoustic efficiency. It is the statistical signature of the spatial desynchronization of wavepackets due to turbulent forcing, a phenomenon that has been referred to as 'jitter' by Cavalieri *et al.* [51] and also modelled by Ffwocs-Williams and Kempton [52]. Cavalieri & Agarwal [48] showed that agreement in average phases and convection velocities obtained using linear models is not a sufficient condition to match the far pressure field of a sound source. A sufficient condition involves matching, in addition to amplitude and phase velocity, the two-point coherence of the source.

Kinematic models, as opposed to dynamic models based on stability theory, are useful in so far as they provide a framework that allows the salient sound-producing flow traits to be understood. Based on experiments, kinematic wavepacket source models have been proposed and their radiated sound field assessed, for example, by Crow [42], Crighton [53], Michalke [31] and Crighton & Huerre [54]. These studies proposed wavepacket models with similar shapes based on single-point measurements and therefore did not consider coherence decay. More recently, using Crow's model [42], Cavalieri *et al.* [44] inferred the single-point wavepacket structure from the single-point statistics of the sound field and found a superdirective wavepacket consistent with the polar structure of the sound field for azimuthal Fourier modes $m = 0, 1$ and 2 and $0.2 \leq St \leq 0.8$. The length of the wavepacket envelope was estimated between 6 and 8 jet diameters and a non-dimensional envelope length of $k_h L = 6$ was found, where k_h is the hydrodynamic wavenumber. The phase speed was taken from a local stability analysis. This model has since been widely used to study both free and installed jet noise [55–58]. Given that the importance of modelling two-point statistics was recognized early by Harper-Bourne [11,12] and by Michalke [59], it is somewhat surprising that no wavepacket models featuring coherence decay were proposed earlier. It is only since the works of Reba *et al.* [60–63] and Cavalieri and Agarwal [48] that wavepacket models featuring coherence decay have been proposed.

Now that it has become clear that the two-point coherence formulation comprises essential wavepacket source characteristics, the following question arises: to what extent are the source model characteristics identified by Cavalieri *et al.* [44] representative of actual wavepackets in the turbulent jet? As with all inverse-like source-identification approaches, which are ill-posed, one can always find a set of parameters that produces the correct sound field, but which may not be compatible with the real source structure.

In light of this, the objective and novelty of the work reported here is to use the two-point model of Cavalieri & Agarwal [48] combined with data from an LES simulation performed using the compressible flow solver 'Charles' [64] to identify and understand the key wavepacket parameters and to evaluate the acoustic radiation of the model, in terms of both directivity and acoustic efficiency. Whereas Cavalieri *et al.* [44] worked from the outside in, i.e. inferring the source structure from the sound field, we here work from the inside out, building the source with information from the computed velocity field, the goal being to effect a quantitative calculation of the sound field using the two-point kinematic model whose parameters are this time extracted directly from the turbulent field. This approach follows the earlier ones by Harper-Bourne [11,12], Goldstein & Kharavan [22], Goldstein & Leib [23], Karabasov *et al.* [20] and Leib & Goldstein [24], except that here we work with a wavepacket model source characterized by a small number of parameters, and we inform this using full-field flow data. The single and two-point acoustic predictions are compared with experiments conducted at the *Bruit et Vent* anechoic facility located in Poitiers, France. We focus the analysis on acoustic results at low polar angles to the jet axis for a single azimuthal mode, $m = 0$, and we show that this approach considerably simplifies the modelling task; furthermore, the acoustic predictions of the model were found to agree with the data to within approximately 2 dB up to $St = 0.5$. Our methodology also builds on previous work by Kopiev & Chernyshev [65] and Kopiev & Chernyshev [66], who performed an azimuthal decomposition of the sound field and explored sound source generation mechanisms of different azimuthal modes using the two-stage correlation model developed by Kopiev & Chernyshev [67]. Wavepacket models featuring coherence decay have also been used by Reba *et al.* [60,63] to make acoustic predictions, although with a different methodology than ours; the authors used data from a near-field microphone array and performed an acoustic extrapolation of the near-field data to the acoustic field by solving the homogeneous wave equation. While their model worked well for supersonic jet conditions, for subsonic Mach numbers, they underpredicted the data by roughly 10 dB at low polar angles.

The kinematic modelling we propose is related to the dynamic models as follows. The shortcomings of linear dynamic models can be overcome by including an inhomogeneous, forcing term, associated with nonlinear interactions understood as the effect of turbulence forcing on wavepackets. A series of studies have explored forced, inhomogeneous models for the Navier–Stokes equations [68–72], addressing the problem in terms of an 'input–output' analysis, where the input corresponds to the forcing and the output to the response modes of the flow, these being connected by the resolvent of the linearized Navier–Stokes equations. More recently, Semeraro *et al.* [73], Towne *et al.* [74] and Towne *et al.* [75] explored the link between resolvent modes and Spectral Proper Orthogonal Decomposition (SPOD) (a frequency domain form of Proper Orthogonal Decomposition) modes in turbulent jets. They show, consistent with the work of Farell & Ioannou [68], that when the linear system is forced with a spatiotemporally white stochastic field, the response modes of the resolvent operator are identical to the SPOD modes of the flow. This is not the case if the forcing is coloured and the difference between SPOD and resolvent modes may help shed light on the nature of the forcing.

This issue prompted us to perform SPOD of the kinematic source model with a view to searching for the acoustically important degrees of freedom of wavepackets that might be used to construct a low-rank representation of the flow. We are interested in finding a reduced-rank description that suffices to provide an accurate description of the two-point structure that is relevant for sound radiation and that the dynamic models need to model correctly if they are to make accurate predictions of sound pressure levels.

Similarly to what was found by Breakey *et al.* [41] and Suzuki [76] in the near pressure field, we show here that a one-mode representation of the Cross-Spectral Density (CSD) of the source is not sufficient to capture all of the acoustically important features and that higher modes are important for sound radiation. But only a small number of modes was necessary to recover the correct wavepacket parameters and sound pressure levels.

The remainder of the paper is organized as follows: In §2, we present the two-point kinematic source model. This is followed, in §3, with the provision of information regarding the LES and acoustic databases. In §4, we describe the procedure used to educe the wavepacket parameters from the LES data. In §5, we compare the acoustic results of the model to experimental data and discuss the discrepancies and the role of the wavepacket parameters. In §6, we present the SPOD analysis and we discuss the possibilities of low-rank models for the description of the acoustically important wavepacket characteristics. Finally, conclusions and hypotheses are discussed in §7.

2. Kinematic model

(a) Basic equations

A generalized expression for an acoustic analogy can be written as

$$\mathfrak{L}(p) = q(\mathbf{x}, t), \tag{2.1}$$

where $\mathfrak{L}$ is a linear operator that depends on the acoustic analogy, p is the pressure and $q(\mathbf{x}, t)$ is the source distribution.

The solution for the pressure, p, is given as

$$p(\mathbf{x}, t) = -\int_{-\infty}^{\infty} \int_{\mathscr{V}} q(\mathbf{y}, \tau) G(\mathbf{x}, \mathbf{y}, t - \tau) \, d\mathbf{y} \, d\tau, \tag{2.2}$$

where $G(\mathbf{x}, \mathbf{y}, t - \tau)$ is the Green's function for the linear operator $\mathfrak{L}$. $\mathbf{x}$ is the observer's coordinates and $\mathbf{y}$ the source's coordinates.

Application of equation (2.2) involves the integration of flow fluctuations, which are stationary random functions and hence are not square-integrable functions. A solution to overcome this issue is to work with the auto and cross-correlations, which are supposed to decay to zero for large separation distances and time delays [77]. The pressure autocorrelation is defined by

$$\overline{p^2}(\mathbf{x}, \tau) = \lim_{T \to \infty} \frac{1}{2T} \int_{-T}^{T} p(\mathbf{x}, t) p(\mathbf{x}, t + \tau) \, dt, \tag{2.3}$$

and that can be expressed, using equation (2.2), as

$$\overline{p^2}(\mathbf{x}, \tau) = \frac{1}{2T} \int_{-T}^{T} \int_{-\infty}^{\infty} \int_{-\infty}^{\infty} \int_{\mathscr{V}} \int_{\mathscr{V}} G(\mathbf{x}, \mathbf{y}_1, t - \tau_1) G(\mathbf{x}, \mathbf{y}_2, t + \tau - \tau_2)$$
$$q(\mathbf{y}_1, \tau_1) q(\mathbf{y}_2, \tau_2) \, d\mathbf{y}_1 d\mathbf{y}_2 d\tau_1 d\tau_2 dt. \tag{2.4}$$

In the following, we follow the development of Goldstein & Leib [23]. We make three changes of variables $\boldsymbol{\eta} = \mathbf{y}_2 - \mathbf{y}_1$, $\tau_3 = \tau_2 - \tau_1$ and $t_1 = t - \tau_1$ and define $\mathscr{R}(\mathbf{y}_1, \boldsymbol{\eta}, \tau_3)$, a two-point time-delayed cross-correlation of the source based on flow quantities,

$$\mathscr{R}(\mathbf{y}_1, \boldsymbol{\eta}, \tau_3) = \frac{1}{2T} \int_{-T}^{T} q(\mathbf{y}_1, \tau_1) q(\mathbf{y}_1 + \boldsymbol{\eta}, \tau_1 + \tau_3) \, d\tau_1. \tag{2.5}$$

The expression for the pressure autocorrelation then becomes:

$$\overline{p^2}(\mathbf{x}, \tau) = \int_{-\infty}^{\infty} \int_{-\infty}^{\infty} \int_{\mathscr{V}} \int_{\mathscr{V}} G(\mathbf{x}, \mathbf{y}_1, t - \tau_1) G(\mathbf{x}, \mathbf{y}_1 + \boldsymbol{\eta}, t + \tau - \tau_2) \mathscr{R}(\mathbf{y}_1, \boldsymbol{\eta}, \tau_3) \, d\mathbf{y}_1 d\boldsymbol{\eta} d\tau_3 dt. \tag{2.6}$$

We also define a modified Green's function, $G'(\mathbf{x}, \mathbf{y}_1, \boldsymbol{\eta}, \tau - \tau_3)$, given by:

$$G'(\mathbf{x}, \mathbf{y}_1, \boldsymbol{\eta}, \tau - \tau_3) = \int_{-\infty}^{\infty} G(\mathbf{x}, \mathbf{y}_1, t_1) G(\mathbf{x}, \mathbf{y}_1 + \boldsymbol{\eta}, t_1 + \tau - \tau_3) \, dt_1. \tag{2.7}$$

Inserting equation (2.7) into equation (2.6), we have

$$\overline{p^2}(\mathbf{x}, \tau) = \int_{-\infty}^{\infty} \int_{\mathscr{V}} \int_{\mathscr{V}} G'(\mathbf{x}, \mathbf{y}_1, \boldsymbol{\eta}, \tau - \tau_3) \mathscr{R}(\mathbf{y}_1, \boldsymbol{\eta}, \tau_3) \, d\mathbf{y}_1 d\boldsymbol{\eta} d\tau_3. \tag{2.8}$$

This equation can be equivalently expressed as:

$$\overline{p^2}(\mathbf{x}, t) = \int_{-\infty}^{\infty} \int_{\mathscr{V}} \int_{\mathscr{V}} G'(\mathbf{x}, \mathbf{y}, \boldsymbol{\eta}, t - \tau) \mathscr{R}(\mathbf{y}, \boldsymbol{\eta}, \tau) \, d\mathbf{y} d\boldsymbol{\eta} d\tau. \tag{2.9}$$

Equation (2.9) gives an expression for the pressure autocorrelation as a function of a Green's function and of the cross-correlation of the source, $\mathscr{R}$. The latter is a function of coordinate vector, $\mathbf{y}$, separation distance, $\boldsymbol{\eta}$ and time delay, τ. Modelling this quantity is not a straightforward task, and this has obliged authors in the past to add free parameters to calibrate their models. The reason is that the modelling requires knowledge of the cross-correlation structure in all of the volume $\mathscr{V}$ where the source is defined; the information about how it varies with all of the components of $\mathbf{y}$, $\boldsymbol{\eta}$ and τ is usually not entirely available from experiments or is limited to certain regions of the jet. This difficulty is true to all acoustic analogies. Here we wish to show that the modelling task is simplified by working in the frequency domain and concentrating on a single azimuthal mode and low polar angles to the jet axis. This is made possible by the homogeneity of the flow in the time and azimuthal directions.

The sound source model we consider is based on the Lighthill's acoustic analogy,

$$\frac{1}{c_0} \frac{\partial^2 p}{\partial t^2} - \nabla^2 p = q_{ij}, \tag{2.10}$$

where $\mathbf{x}$ denotes spatial coordinates, t is time, p is the pressure, c_0 is the ambient speed of sound and q is Lighthill's tensor, given by [31],

$$q_{ij} = \frac{\partial^2}{\partial x_i \partial x_j}[\rho u_i u_j - v_{ij}] + \frac{1}{c_0^2} \frac{\partial^2}{\partial t^2}[p - c_0^2 \rho], \tag{2.11}$$

where ρ is the density of the fluid, u is the velocity and v_{ij} is the viscous term. Here we focus only on the q_{11} term, which has been shown in previous studies to constitute an appropriate simplification for calculation of sound radiation to low polar angles [44,53,55]. Moreover, we also use the conclusions of the studies of Freund [5], Bodony & Lele [78] and Colonius & Freund [6] to further simplify the source description. Freund [5] and Bodony & Lele [78] showed, by means of DNS and LES simulations, respectively, that at low Strouhal numbers ($St < 0.5$) and polar angles, noise generation is dominated by the linear part of Lighthill's tensor in a Mach 0.9 jet; furthermore, they showed that over the same Strouhal number and polar-angle range, the momentum term, $\rho u_i u_j$, is dominant over the entropic term, $[p - c_0^2 \rho]$. As for the viscous term, Colonius & Freund [6] found it to be negligible to the sound field of a jet with a Reynolds number as low as 2000. In light of these results, we choose to drop the viscous and entropic terms and to only model the linearized part of the stress tensor. This compromises the performance of the model at higher Strouhal numbers and polar angles. However, our main objective here is to explore a simplified model with a view to providing insight into sound generation by wavepackets, hence the main message of this study is not affected by these simplifications. The Lighthill stress tensor then reduces to

$$q_{11} = \frac{\partial^2}{\partial x^2}[2\rho \bar{u}_1 u_1'], \tag{2.12}$$

where $\bar{u}_1$ and u_1' are the streamwise mean and fluctuation velocities, respectively.

The solution to Lighthill's acoustic analogy for the m-th azimuthal pressure component in the frequency domain for an observer in the far field was given by Michalke [31],

$$p_m(R, \theta, \omega) = \frac{i^m e^{-ik_a R} k_a^2 \cos^2 \theta}{2R} \iint Q_m(x, r, \omega) e^{ik_a x \cos \theta} J_m(k_a r \sin \theta) r \, dr dx, \tag{2.13}$$

Table 1. Values of $J_0(2\pi\, StMr/D \sin\theta)$.

	$St = 0.3$		$St = 0.5$		$St = 0.7$	
	$\theta = 20°$	$\theta = 90°$	$\theta = 20°$	$\theta = 90°$	$\theta = 20°$	$\theta = 90°$
$r/D = 0.2$	0.99	0.99	0.99	0.98	0.99	0.97
$r/D = 1$	0.98	0.86	0.95	0.64	0.91	0.36
$r/D = 2$	0.94	0.51	0.82	−0.06	0.67	−0.38

where the observer is in polar coordinates and the source in cylindrical coordinates. k_a is the acoustic wavenumber, J_m is the Bessel function of the first kind and order m. Q is the Fourier transform of the argument of the differential operator of q_{11} and the double derivative was passed to the Green's function using the divergence theorem, as demonstrated by Goldstein [79].

The power spectral density of the pressure, which is the Fourier transform of the pressure autocorrelation defined in equation (2.9), is then given by

$$\langle p_m(R,\theta,\omega) p_m^*(R,\theta,\omega)\rangle = (-1)^m \mathrm{i}^{2m} \frac{k_a^4 \cos^4\theta}{4R^2}$$

$$\iiiint \langle Q_m(x_1,r_1,\omega) Q_m^*(x_2,r_2,\omega)\rangle \mathrm{e}^{\mathrm{i}k_a\cos\theta(x_1-x_2)} J_m(k_a r_1 \sin\theta) J_m(k_a r_2 \sin\theta) r_1 r_2\, \mathrm{d}r_1 \mathrm{d}r_2 \mathrm{d}x_1 \mathrm{d}x_2, \quad (2.14)$$

where the symbols $\langle.\rangle$ denote expected value. The quantity $\langle Q_m(x_1,r_1,\omega)Q_m^*(x_2,r_2,\omega)\rangle$ is the cross-spectral density of the source and is equivalent to the Fourier transform of the cross-correlation, $\mathcal{R}$.

In this work, we are interested in the $m = 0$ axisymmetric mode. For small values of the argument of the Bessel function, $k_a r \sin\theta = 2\pi StMr/D \sin\theta \ll 1$, J_0 is approximately 1, and the Bessel function term can be neglected. Table 1 shows values of the argument of the Bessel function for the range of Strouhal numbers, radial positions and polar angles we consider in this work. We can see that the accuracy of the results at high angles, which is already limited by the linearization of the source, is clearly affected by neglecting the Bessel function. For $St = 0.5$ and higher, this simplification begins to affect also low polar angles. More considerations about the limits to this simplification and how it affects the present modelling strategy are made in §5.

The expression for the axisymmetric component of the PSD then becomes:

$$\langle p_0(R,\theta,\omega) p_0^*(R,\theta,\omega)\rangle = \frac{k_a^4 \cos^4\theta}{4R^2}$$

$$\iiiint \langle Q_0(x_1,r_1,\omega) Q_0^*(x_2,r_2,\omega)\rangle \mathrm{e}^{\mathrm{i}k_a\cos\theta(x_1-x_2)} r_1 r_2\, \mathrm{d}r_1 \mathrm{d}r_2 \mathrm{d}x_1 \mathrm{d}x_2. \quad (2.15)$$

Our approach then consists in using a line-source function, $S(x_1,x_2,\omega)$, to model the radially integrated source,

$$\iint \langle Q(x_1,r_1,\omega) Q^*(x_2,r_2,\omega)\rangle r_1 r_2\, \mathrm{d}r_1 \mathrm{d}r_2 \approx S(x_1,x_2,\omega). \quad (2.16)$$

The subscripts referring to azimuthal mode have been dropped for convenience, but hereafter, all of the flow and acoustic information discussed refers to the axisymmetric mode.

We can see the modelling advantage of only taking into account the $m = 0$ azimuthal mode and concentrating at low polar angles and Strouhal numbers: instead of having to model the full cross-spectral density (or the cross-correlation, its counterpart in time domain) and how it varies with source position and separation distance (equation (2.9)), here we are left with the much simpler task of modelling the two-point statistics for a pair of points (x_1, x_2) in the streamwise direction. It is worth emphasizing that this approach is only possible due to the significant amount of information provided by the LES, which contains the radial structure of the source and thus allows the radial integration of equation (2.16).

The present modelling methodology is different from past studies that used a wavepacket line-source approach [44,51,58,80] to the extent that we do not choose a specific radial position from which to extract flow information and build the model; instead, we model the radially integrated Lighthill stress tensor, so that equation (2.16) uses all the information available from the numerical database and yields a line-source model that contains information about the radial structure of the source.

(b) Wavepacket source model

Here we use modified versions of the model of Cavalieri & Agarwal [48] for the source, which comprises a line-source wavepacket of CSD, $S(x_1, x_2, \omega)$, with modulated amplitude and coherence. The coherence and amplitude envelopes were modified so as to better represent the flow of information extracted from the simulation. For the coherence envelope (last term on the right-hand side of equation (2.17)), we used a model proposed by Jordan *et al.* [81] and O'Hara *et al.* [82], which consists in the convolution of Gaussian and exponential functions, as opposed of the Gaussian used by Cavalieri & Agarwal [48]. The reason for this, as discussed in §4, is that the convolution allows an accurate description of coherence at small separation distances. Moreover, two envelope functions have been used: a standard Gaussian used in past studies [44,48,53,54] and a modified Gaussian that has an asymmetric decay rate. Asymmetric wavepacket models have also been explored by Papamouschou [83] and Koenig *et al.* [84]. The expression for the CSD with a Gaussian envelope is given as

$$S(x_1, x_2, \omega) = A(\omega) \exp[ik_h(\omega)(x_1 - x_2)] \exp\left[-\frac{(x_1 - x_0(\omega))^2}{L(\omega)^2} - \frac{(x_2 - x_0(\omega))^2}{L(\omega)^2}\right] \gamma^2(x_1, x_2, \omega) \quad (2.17)$$

where $k_h(\omega)$ is the hydrodynamic wavenumber, $L(\omega)$ is the characteristic wavepacket length, and $\gamma^2(x_1, x_2, \omega)$ is the coherence function. $A(\omega)$ is a term that sets the amplitude of the source. It is taken as the maximum amplitude of the integrated source tensor, which occurs at the streamwise position corresponding to the centre of the wavepacket, $x_0(\omega)$, which is itself a function of frequency.

The coherence function, $\gamma^2(x_1, x_2, \omega)$, is given as

$$\gamma^2(x_1, x_2, \omega) = \frac{1}{2L_{c_1}} \int_{-\infty}^{\infty} e^{-(|x_1 - x_2 - \eta|/L_{c_1})} e^{-((x_1 - x_2)^2/L_{c_2}{}^2)} \, d\eta, \quad (2.18)$$

where L_{c_1} and L_{c_2} are the lengthscales associated with the exponential and Gaussian functions, respectively and are function of ω.

A Gaussian function provides a good approximation for the amplification part of the amplitude shapes (this is shown in §4, figure 4). However, the decaying part is asymmetric and a Gaussian is not able to accurately represent the wavepacket envelope. Thus, an asymmetric Gaussian envelope has also been used to fit the envelopes, given by the function

$$f(x) = \frac{1}{L_{as}} e^{x^2/L_{as}^2} \operatorname{erfc}\left[\frac{\alpha x}{\sqrt{2}L_{as}}\right], \quad (2.19)$$

where L_{as} is a characteristic length of the asymmetric envelope, α is a parameter controlling the decay part of the function and erfc is the complementary error function. The CSD with the asymmetric envelope becomes

$$S(x_1, x_2, \omega) = A(\omega) \frac{1}{L_{as}(\omega)^2} \exp[ik_h(\omega)(x_1 - x_2)] \exp\left[-\frac{(x_1 - x_0(\omega))^2}{L_{as}(\omega)^2} - \frac{(x_2 - x_0(\omega))^2}{L_{as}(\omega)^2}\right]$$

$$\times \operatorname{erfc}\left[\frac{\alpha(\omega)(x_1 - x_0(\omega))}{\sqrt{2}L_{as}(\omega)}\right] \operatorname{erfc}\left[\frac{\alpha(\omega)(x_2 - x_0(\omega))}{\sqrt{2}L_{as}(\omega)}\right] \gamma^2(x_1, x_2, \omega). \quad (2.20)$$

Both models are based on two-point statistics of the flow since these take into account coherence decay. By making $L_{c_{1,2}} \to \infty$, one eliminates the two-point dependence and obtains a

9

royalsocietypublishing.org/journal/rspa   *Proc. R. Soc. A* **475**: 20190199

model based on single-point statistics. The parameters highlighted in equations (2.17) and (2.20) in red may then be educed from the simulation database after performing the integrals in the radial direction.

Therefore, using equations (2.17) or (2.20) once the parameters have been educed, one can evaluate the far-field radiation of the model source through the following equation:

$$\langle p(R,\theta,\omega)p^*(R,\theta,\omega)\rangle = \frac{k_a^4 \cos^4\theta}{4R^2} \iint S(x_1,x_2,\omega)e^{ik_a\cos\theta(x_1-x_2)}\,\mathrm{d}x_1\mathrm{d}x_2. \tag{2.21}$$

It is worth emphasizing that this model is contained in the more general source description given by equation (2.9), and explored, for example, by Kharavan *et al.* [26], Tam & Auriault [25], Self [21], Goldstein & Kharavan [22], Goldstein and Leib [23] and Leib and Goldstein [24], Kopiev and Chernyshev [65]. Wavepackets, like the source models proposed in those studies, are also of quadrupolar nature but are characterized by longer space scales. By focusing on these specific flow entities, given their now demonstrated importance for sound radiation, we obtain a simplified line-source description that requires a relatively small number of parameters.

3. Databases

A large-eddy simulation of an isothermal Ma = 0.4 turbulent jet has been performed using the compressible solver 'Charles' [85]. The nozzle geometry and flow parameters reproduce the experimental setup of the *Bruit et Vent* noise facility of the PPRIME institute, located in Poitiers, France, and studied in previous studies [19,35,44]. The Reynolds number based on the jet diameter is 4.6×10^5, and synthetic turbulence is used in the simulation to mimic the effect of the boundary layer trip present in the experiment at a streamwise distance of $x/D = 2.5$ upstream of the jet exit. The simulation has been run for a total time of 2000 acoustic time units, where the acoustic time is defined as tc_0/D. The unstructured grid was interpolated to a cylindrical grid that covers a volume extending from $0 \le x/D \le 30$, $0 \le r/D \le 6$, $0 \le \Phi \le 2\pi$. Schmidt *et al.* [85] used this same database to perform spectral proper orthogonal decomposition and resolvent analysis with a view to study the low-rank behaviour of turbulent jets. More details about the numerical method and meshing strategy can be found in Brès *et al.* [46].

The acoustic measurements were performed with an azimuthal ring array of diameter 14.3D that contained 18 microphones. It is the same array previously used by Piantanida *et al.* [56]. The ring was displaced in the axial position in the range $0D \le x \le 39D$ so as to vary the polar angle, covering a cylindrical surface. This configuration allowed the decomposition of the pressure signal into Fourier modes up to $m = 9$. A schematic of the acoustic experiment is shown in figure 1. Both flow and acoustic data have been Fourier transformed in the azimuthal direction in order to extract the $m = 0$, axisymmetric mode.

Figure 2 compares the LES with experimental data for the same jet: flow statistics are compared with PIV data from Jaunet *et al.* [19] and sound pressure levels of the full sound field as a function of polar angle are compared with measurements made using the experimental set-up described above. The sound field is computed from the LES by means of a permeable formulation of the Ffowcs Williams & Hawking equation in the frequency domain [46,64]. Mean flow and rms profiles are in good agreement with the PIV data. The experimental data seem to underpredict the rms levels of the LES near the nozzle, which can be explained by the low level of the magnification factor of the PIV at this position, as discussed by Jaunet *et al.* [19]. Directivities computed from the simulation are also in good agreement with experimental data.

4. Parameter eduction

In what follows we describe the procedure adopted in order to educe the parameters necessary to build the CSD models given by equations (2.17) and (2.20) from the LES data. The optimal parameters were selected using the MATLAB® *fminsearch* routine, a nonlinear least-squares algorithm in which the error between data and model was minimized using the Nelder–Mead
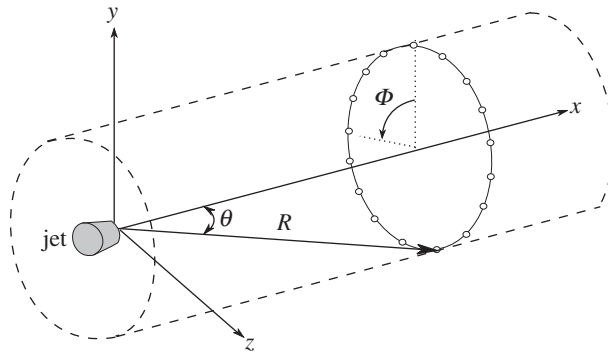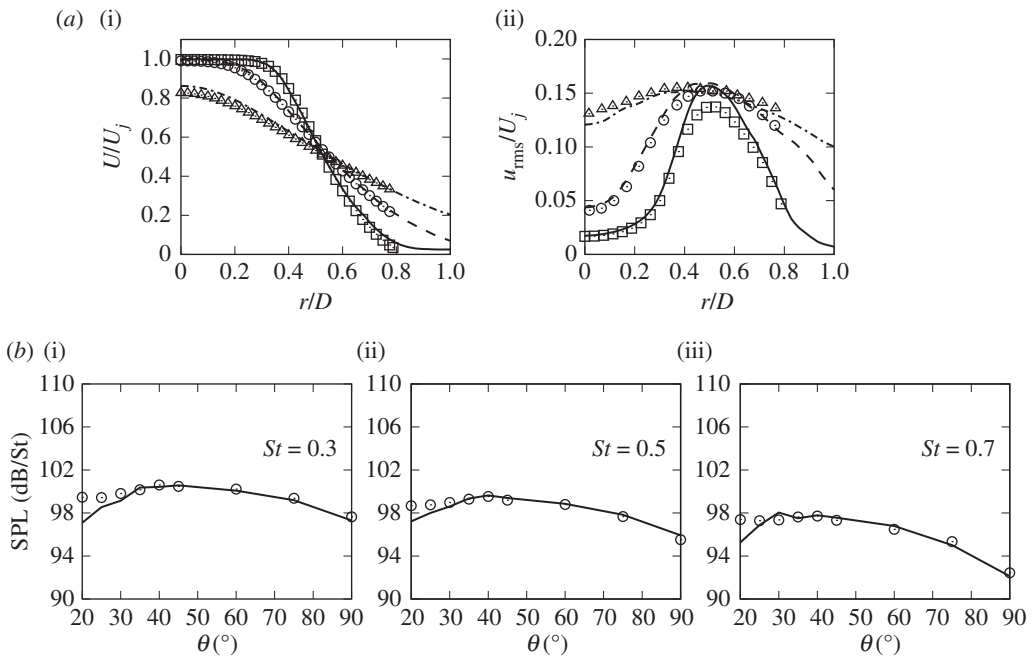
Figure 1. Schematic of microphone array.

Figure 2. (*a*) Mean flow (i) and rms (ii) radial profiles obtained from PIV (points) and LES (lines). Profiles at three streamwise stations are shown: $x/D = 2.5$ (solid line and squares); $x/D = 4.5$ (dashed-line and circles); $x/D = 8$ (dashed-dotted-line and triangles). (*b*) Directivity plots for three Strouhal numbers with an observer in the cylindrical surface delimited by the microphone array (figure 1). Circles: experimental data; solid line: LES far-field prediction computed using the Ffowcs Williams & Hawkings equation.

simplex method. The data consist of the full source CSD, $\langle Q(x_1, r_1, \omega) Q^*(x_2, r_2, \omega) \rangle$, dependent on two axial coordinates, two radial coordinates and frequency. Prior to the eduction, the data are radially integrated twice and the model is created based on the line-source that results from this operation, given by equation (2.16). Thus, all of the parameters have been educed for the integrated source, and the information regarding the radial structure of the source is, so to speak, contained in these and in the amplitude term. Since all the radial structure of the source available is taken into account, it is not necessary to pick a specific radial position at which to educe the parameters, unlike other studies that use a line-source approach [44,51,58,80].
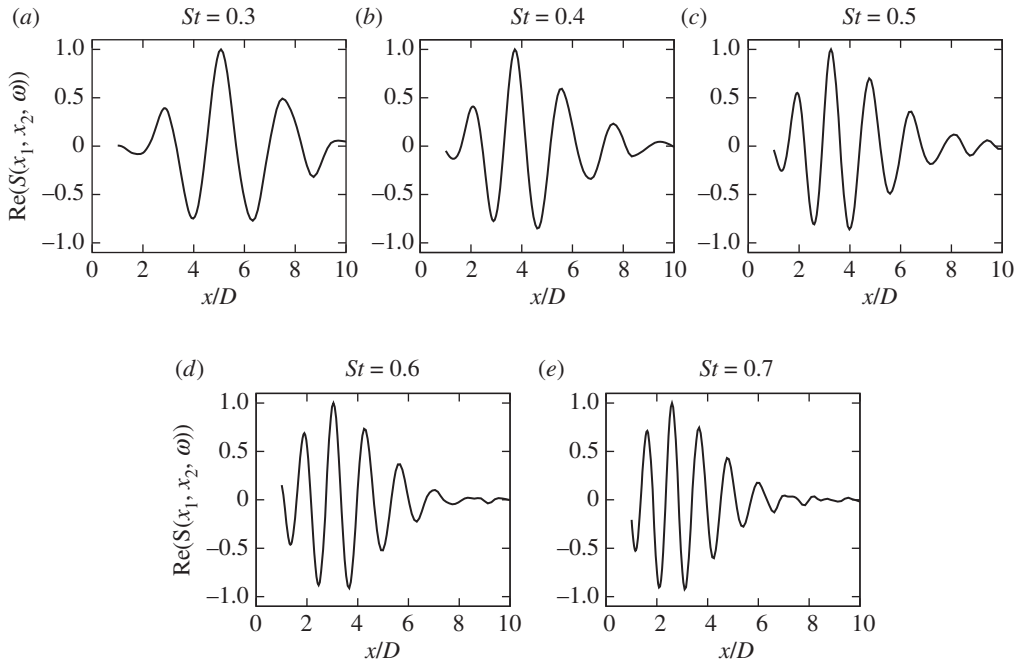
Figure 3. Radially integrated CSD issued from the LES for different Strouhal numbers. Reference point is at $x_0(\omega)$. Levels have been normalized by the maximum value at each Strouhal number.

Figure 3 shows the real part of the radially integrated CSD, $S(x_1, x_2, \omega)$, issued from the LES for $0.3 \leq St \leq 0.7$ with the reference point at the peak of the wavepacket, x_0. The wave-like character of the source term of Lighthill's acoustic analogy is evident, which motivates the modelling efforts of the present study.

(a) Wavepacket characteristic length, L

The wavepacket characteristic length, L, was extracted by fitting the PSD of the velocity fluctuation signal with an envelope function. Two envelopes were used: one with a Gaussian form, which corresponds to the model of Cavalieri & Agarwal [48] and a second one with an asymmetric Gaussian form, which accounts for different growth and decay rates. The Gaussian envelope may be obtained by making $x_2 = x_1$ in equation (2.17).

$$S_{\text{sym}}(x_1, \omega) = A(\omega) \exp\left[-\frac{2(x_1 - x_0(\omega))^2}{L(\omega)^2} \right], \tag{4.1}$$

where the amplitude term is the direct result of the double radial integration performed with equation (2.16). This function provides a reasonable fit of radially integrated power spectral densities for the growth part of the wavepacket; however, downstream of the peak the agreement becomes poorer, and the Gaussian fit does not represent the data correctly. Hence, here we propose a modified Gaussian function that takes into account the asymmetry of the wavepacket. This function can be obtained by setting $x_2 = x_1$ in equation (2.20),

$$S_{\text{asym}}(x_1, \omega) = A(\omega) \frac{1}{L_{\text{as}}(\omega)^2} \exp\left[-\frac{2(x_1 - x_0(\omega))^2}{L_{\text{as}}(\omega)^2} \right] \text{erfc}^2\left[\frac{\alpha(x_1 - x_0(\omega))}{\sqrt{2}L_{\text{as}}(\omega)} \right]. \tag{4.2}$$

One can observe, in figure 4, that the asymmetric envelope provides a better match for the data in the decaying part on the envelope, where the Gaussian envelope significantly underpredicts
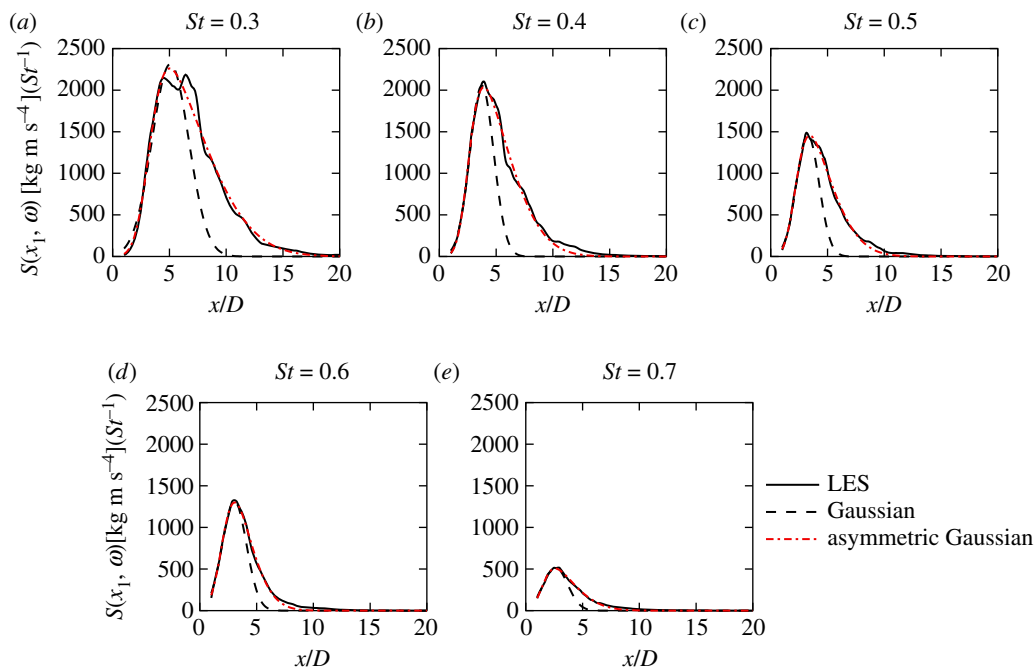
Figure 4. PSD of the source and fitted Gaussian and asymmetric envelopes. (Online version in colour.)

the data. The acoustic radiation of the wavepacket model using both envelopes will be discussed in §5.

(b) Hydrodynamic wavenumber, k_h

The hydrodynamic wavenumber and the phase speed are related through

$$U_c(x_1, \omega) = \frac{\omega}{k_h} = \omega \left(\frac{\partial \phi}{\partial x_2} \right)^{-1}, \tag{4.3}$$

where $\phi(x_1, x_2)$ is the phase shift, obtained as the argument of the CSD. This expression gives the phase speed for reference point x_1 as a function of the rate of change of ϕ with the separation distance from two points. We found this rate of change to be approximately constant in the LES data so that the phase speed was educed from the simulation database by fitting the phase with a linear regression. Figure 5 shows the space–frequency variation of the phase speed. One can observe that the phase speed increases with increasing streamwise position and converges to a value of approximately $U_c/U_j = 0.77$. Harper-Bourne [12] and Morris & Zaman [13] have used a power-law of the form $U_c/U_j = a \ln St + b$ to model the variation of the phase speed with Strouhal number. Here we use the same function to take into account the variation of phase speed with reference position, x_1. The fit can also be seen in figure 5.

(c) Coherence lengths, L_{C_1}, L_{C_2}

The magnitude-squared coherence of the radially integrated source term $S(x_1, x_2, \omega)$, is given as,

$$\gamma^2(x_1, x_2, \omega) = \frac{|\langle S(x_1, x_2, \omega) \rangle|^2}{\langle |S(x_1, \omega)|^2 \rangle \langle |S(x_2, \omega)|^2 \rangle}, \tag{4.4}$$

where $S(x_1, \omega)$ and $S(x_2, \omega)$ are the PSDs at points x_1 and x_2, respectively.
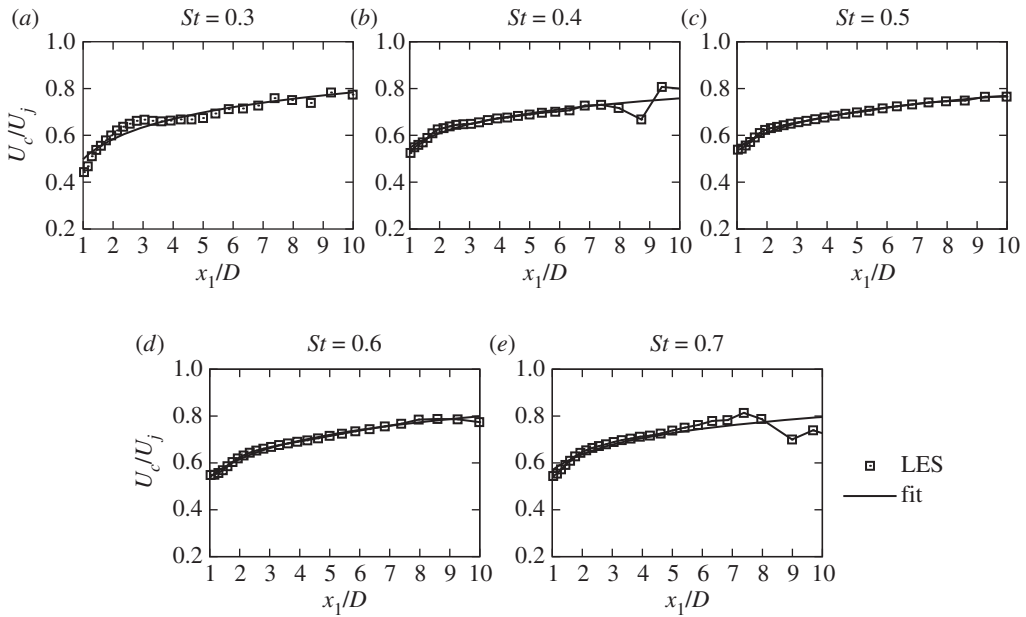
Figure 5. Phase velocity as a function of streamwise reference point, x_1, for different Strouhal numbers and power-law fit.

Jaunet *et al.* [19] used an exponential function to fit coherence decay for a $Ma = 0.4$ jet; however, this function does not provide a correct description of coherence for values of separation distance $\Delta x \rightarrow 0$. Jordan *et al.* [81] and O'Hara *et al.* [82] have proposed, for the two-point correlation, a function given by the convolution of an exponential and a Gaussian. This function has the interesting property of keeping the decay rate of an exponential while providing a zero slope at $\Delta x = 0$. In this work, we use the function of Jordan *et al.* [81], given by equation (2.18), to fit the coherence of the LES data and obtain the two parameters that control the decay rate of the curve, L_{c_1} and L_{c_2}. Figure 6 shows the magnitude-squared coherence as a function of streamwise separation distance for various Strouhal numbers and the fitted function. The reference position was set at the wavepacket peak, x_0. The zero slope at $\Delta x = 0$ can clearly be observed in the data, whence the use of the convolution function. Tam & Auriault [25] and Kopiev & Chernyshev [86] have shown that a sharp behaviour of the correlation function near $\Delta x = 0$ is important for a correct modelling of the broad-band spectra typical of high polar angles. Since this feature is not present in the T_{11} term of Lighthill's tensor, here we argue that it is somewhat less important for sound radiation at low polar angles to the jet axis.

The decay rate of coherence has been found to vary considerably with reference position, x_1. Figure 7 shows the variation of L_{c_1}, the parameter that controls the global decay rate of coherence, as a function of x_1. This spatial dependence has been taken into account by fitting the coherence length with high-order polynomials. L_{c_2}, which corrects the slope of coherence at small separation distances, has been found to be less sensitive to streamwise coordinate. The search for a general scaling for coherence lengths and an expression for their space-frequency dependence is something that will be considered in future work.

(d) Comparison of educed parameters with previous wavepacket models

Cavalieri *et al.* [44] used a Gaussian wavepacket source model based on single-point statistics of the sound field; coherence decay was thus not accounted for. As mentioned in the introduction, because of the ill-posed nature of this inverse problem, one may find more than one set of parameters that produce a source consistent with sound radiation from experimental results.
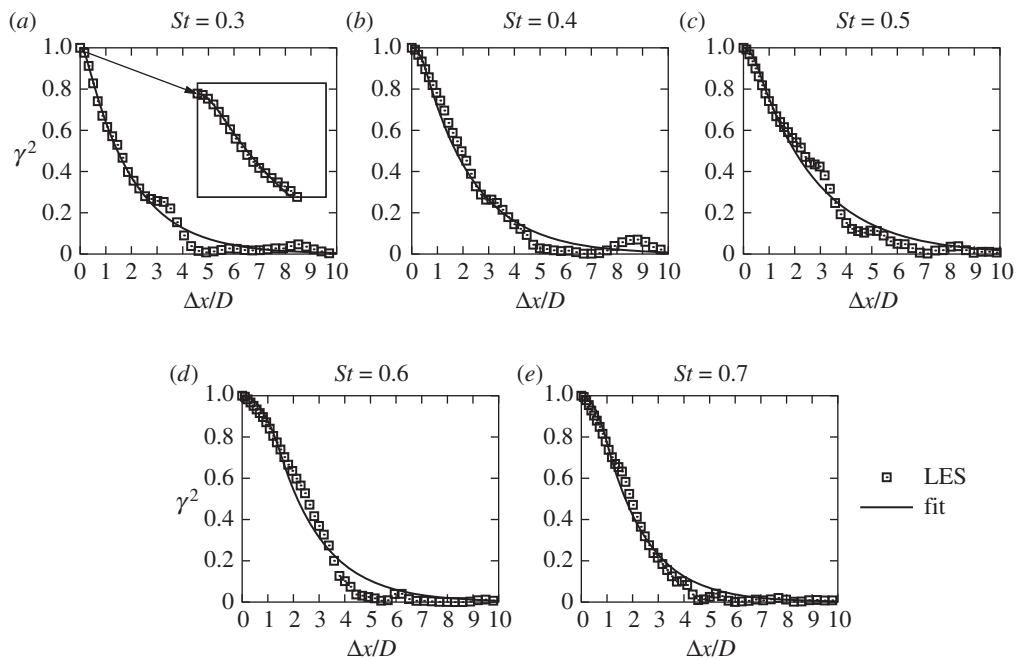
Figure 6. Magnitude-squared coherence of the LES data and fitted curves.
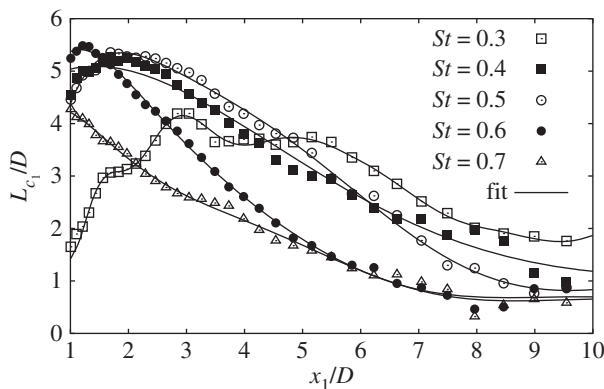

Figure 7. L_{c_1} as a function of reference point and polynomial fitting for various Strouhal numbers.

Table 2. Wavepacket parameters at $St = 0.2$, educed at the wavepacket peak, x_0.

present study				Cavalieri et al. [44]			
$k_h L$	L/D	U_c/U_j	L_{c_1}/D	$k_h L$	L/D	U_c/U_j	L_{c_1}/D
8.97	4.52	0.68	2.49	6.50	3.10	0.6, 0.97	—

These source parameters may not correspond to those of the jet however; the fact that the single-point model lacks coherence decay means that its effect is, so to speak, 'hidden' in the set of parameters found such that the correct sound field is obtained. Indeed, the value found by Cavalieri et al. [44] for the source characteristic length L/D is underestimated with respect to the values educed from the LES data, as shown in table 2; since that work did not consider coherence
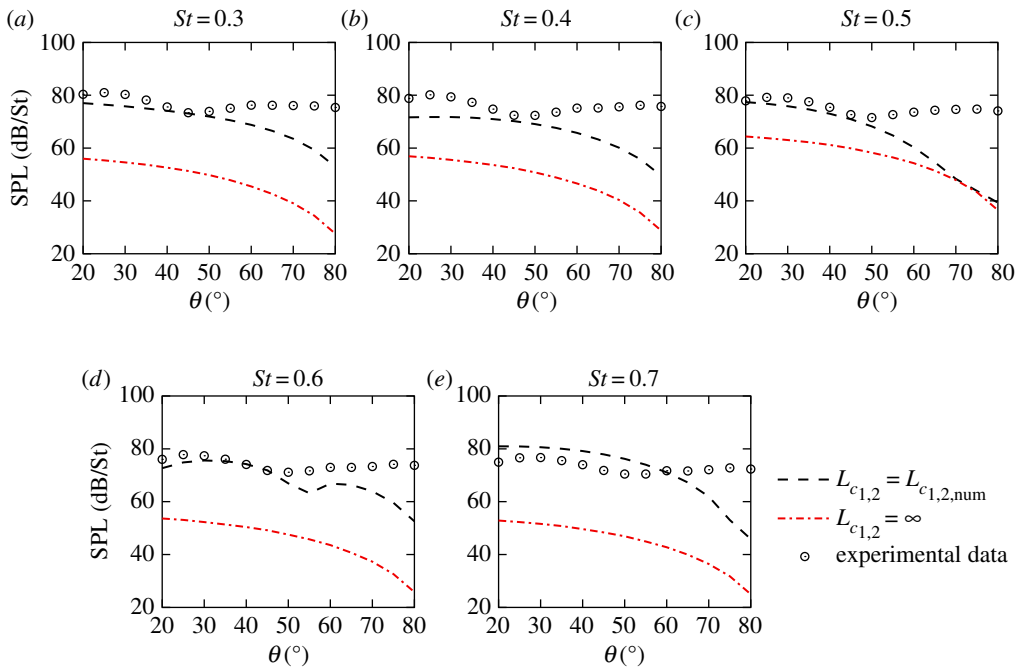
Figure 8. Comparison between sound radiated by single- and two-point wavepacket models and experimental data. The models have a Gaussian amplitude envelope. (Online version in colour.)

decay in the source, it is possible that the lower value of L/D in Cavalieri *et al.* [44] compensates for the effect of the coherence lengthscale in an effective length (such as the modified length L_m in Cavalieri and Agarwal [48]). Also, the phase speeds identified in the LES data are significantly lower than that found from the stability analysis in that work, which was based on a mean velocity profile in the near-nozzle region, where, as can be seen in figure 5, the phase speeds are considerably lower than those observed in most regions of the jet. In table 2, we compare the single-point 'inverse' model of Cavalieri *et al.* [44] with the 'direct' two-point model considered in this work at $St = 0.2$.

5. Acoustic radiation of single- and two-point source models

Here we compare the acoustic fields generated by single and two-point wavepacket models through equation (2.21), where the single-point model is computed by setting $L_{c_{1,2}} = \infty$ in equation (2.17), considering the model with a Gaussian envelope. Figure 8 shows the SPL in dB/St generated by both models, using Gaussian amplitude envelopes, compared with experimental data for the $m = 0$ azimuthal mode at Strouhal numbers $St = 0.3 - 0.7$. Despite the implications of only modelling the linear part of the Lighthill tensor at high polar angles, as evoked in §2, we show the results up to $80°$. It is clear that, if coherence decay is neglected, as is the case for the single-point model, the SPL generated significantly underpredicts the experimental data. Other studies based on dynamic wavepacket modelling have come to a similar conclusion [41,47,49,50]. This further illustrates that the effect of coherence decay was somewhat hidden in, or compensated for by, the single-point parameters estimated from the acoustic field by Cavalieri *et al.* [44]. It must be emphasized that the acoustic data are measured with the observer on the cylindrical surface delimited by the microphone array. This does not correspond to a true polar reference frame, since the distance between source and observer decreases with increasing polar angle; for this reason, the SPL decay rate with polar angle is smaller than that observed by [44].
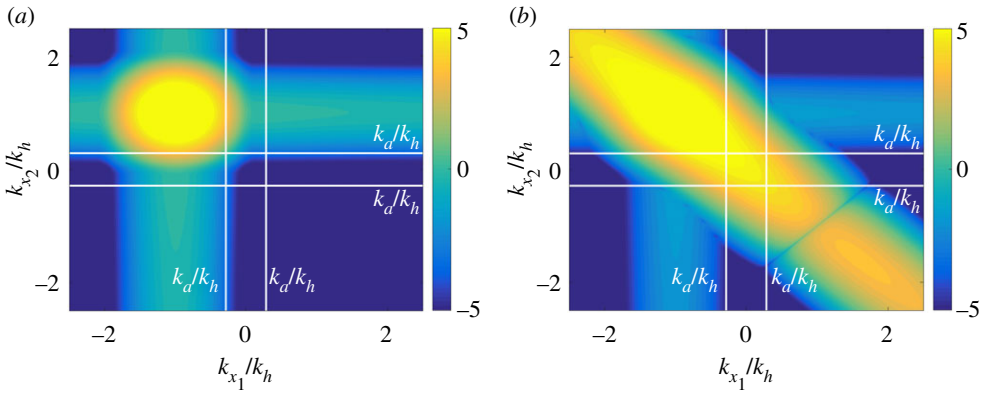
Figure 9. Fourier transform of CSD in wavenumber space at $St = 0.3$. (*a*): source with unit coherence; (*b*): source with coherence modulation. Levels are in dB scale. (*a*) $L_{C_{1,2}} = \infty$, (*b*) $L_{C_{1,2}} = L_{C_{1,2,\text{num}}}$. (Online version in colour.)

In order to understand the effect of coherence on the source structure and sound radiation efficiency, it is interesting to look at the CSD in wavenumber space. Figure 9 shows a comparison of the spatial Fourier transform of the CSD of a source with unit coherence and another with coherence decay at $St = 0.3$. k_{x_1} and k_{x_2} are wavenumbers corresponding to the x_1 and x_2 directions, respectively. From equation (2.21), which can be recognized as a double spatial Fourier transform, we realize that only the wavenumbers that are in the range $|k_{x_1}| \leq k_a$ and $|k_{x_2}| \leq k_a$ contribute to sound radiation. From the relation of wavenumber and phase speed given by equation (4.3), we have,

$$U_{c_1} > c \tag{5.1}$$

and

$$U_{c_2} > c, \tag{5.2}$$

where c is the sound speed and U_{c_1} and U_{c_2} are the phase speeds associated with wavenumbers k_{x_1} and k_{x_2}, respectively. This shows that only wavenumbers with supersonic associated phase speeds contribute to far-field radiation.

These conditions can also be written as

$$\frac{|k_{x_1}|}{k_h} < M_c \tag{5.3}$$

and

$$\frac{|k_{x_2}|}{k_h} < M_c, \tag{5.4}$$

as shown by Cavalieri & Agarwal [48]. The wavenumbers respecting this inequality have been referred to as 'acoustically matched' [34,53]. The radiating region of the spectrum is illustrated in figure 9 by the square delimited by the acoustic wavenumber. One can observe that, for the source with no coherence decay, all of the significant energy of the source is contained outside of the radiating region (figure 9*a*). We thus understand the significant difference in the acoustic efficiency. The effect of coherence decay is to stretch the source in wavenumber space, such that a more significant part of its energy is contained in the radiating part of the spectrum (figure 9*b*).

Although the two-point model with Gaussian amplitude envelope produces acoustic results that are much closer to the data, there are some discrepancies in SPL and directivity with respect to the experimental data, specially at low St. In what follows, we explore the differences between sound radiation of the Gaussian and asymmetric wavepackets. Figure 10 compares the SPL generated by both models with the acoustic data.

We also show the sound radiation obtained by directly applying equation (2.15) on the linearized q_{11} term directly computed from the LES data. These results (the black solid lines in
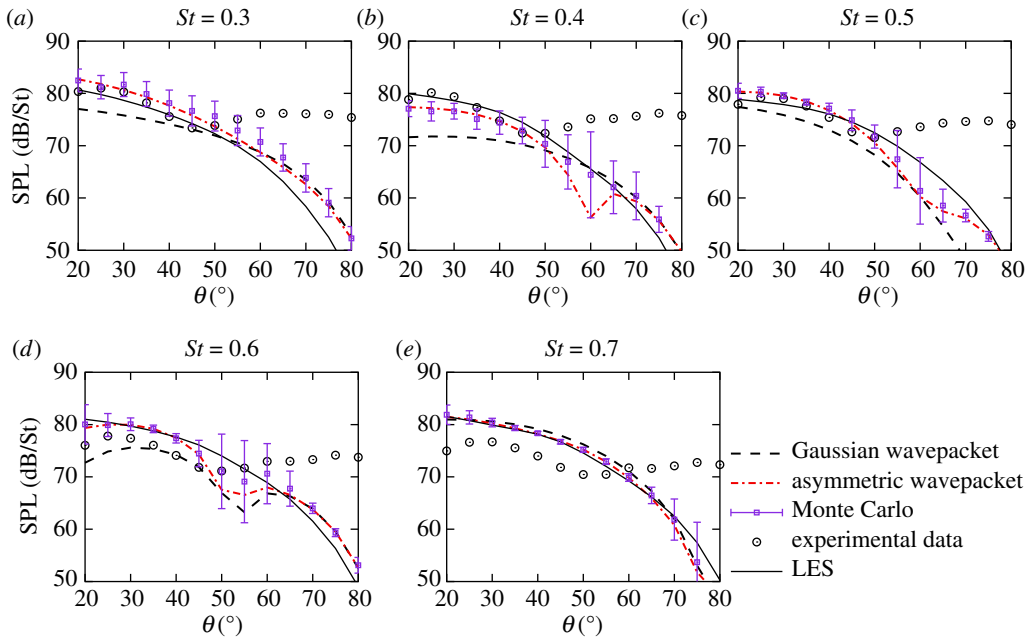
Figure 10. Sound radiation by sources with Gaussian an asymmetric amplitude envelopes. The error bars are centred at the mode of the sample values computed in the Monte Carlo simulation. (Online version in colour.)

figure 10) can be thought of as the best ones that may be attained by the model using the current approach, because they correspond to the fully computed CSD matrix, without any modelling. We can see the agreement between the sound radiation computed with this method and the acoustic data is quite good up to $St = 0.5$. Beyond that St, overpredictions of approximately 5 dB are observed. This breakdown at higher St can be explained by the simplification made in equation (2.15), in neglecting the radial structure of $J_0(k_a r \sin \theta)$. This term, named 'jet thickness' by Michalke [31] accounts for radial interferences of the sources within the jet, and its neglect yields an increase in sound radiation. As shown in table 1, neglecting the structure of the Bessel function starts to be problematic at low polar angles for $St > 0.5$; for instance, taking $r/D = 2$ as the integration limit of equation (2.14) leads to an overestimation of approximately 20% in $J_0(k_a r \sin \theta)$ for low θ. The results of the LES sound radiation depicted in figure 10 suggest that $St = 0.5$ is indeed the upper limit of the methodology we consider here.

It may also be observed that the asymmetric wavepacket model provides better matches with the data, specially at lower St, both in terms of amplitude and directivity. The sound radiation of the model is within 2 dB of the data up to $\theta = 50°$. This reveals that a correct representation of the envelope is also a key aspect to be considered in order to make accurate acoustic predictions. As St is increased the difference between the two types of envelope become less marked, as seen in figure 4, and the results of the two models become closer. At high polar angles, the agreement breaks down due to the simplifications made in the derivation of the model but also due to the lack of the other terms of the Lighthill stress tensor. As a matter of fact, one should expect the importance of the q_{11} term to be reduced with increasing polar angle due to the $\cos^4 \theta$ directivity factor in equation (2.21). Modelling of these terms, which is beyond the scope of the work presented, is something to be considered for future work.

In order to assess the robustness of the model regarding its parameters, a Monte Carlo simulation was carried out for the model with the asymmetric envelope. We assumed that the parameters could vary at the same time by $\pm 10\%$ about the values educed from the LES and that they followed a normal probability distribution; then the sound field was computed for 1000 random combinations of the parameters. The results of the Monte Carlo simulation can also be

seen in figure 10, which shows the error bars centred around the most frequent value found in the simulation. It can be seen that the results of the asymmetric model are well within the range delimited by the error bars and are close to the most frequent value of the sample values computed. The maximum error found was approximately 3 dB up to $\theta = 50°$, and it increases in the polar range at which the model is no longer suitable for making acoustic predictions. These results reveal a certain robustness and the capacity of making accurate acoustic predictions even if numerical errors were to introduce errors in the eduction of the parameters.

The results of the kinematic models identify the parameters that dynamic models should be crafted to correctly predict. The phase speed is theoretically available from linear stability models. But the decay rate of the amplitude envelope, the coherence decay and the global amplitude are not readily available from such calculations. These parameters can only be determined by including an inhomogeneous term in the linearized equations, in which nonlinear forcing will fix amplitude and determine the decay rate and coherence decay. In this framework, the resolvent of the linear operator is a key element, that determines how nonlinear interactions force the linear waves. Studies [73,74] have shown that there exists a close link between the optimal forcing and response modes of the resolvent operator and SPOD modes of wavepacket CSD. We keep this in mind in the following section where we perform SPOD of the source CSD with the asymmetric envelope (the one that gives more accurate acoustic predictions) with a view to exploring the possibility of low-rank modelling of the key source parameters highlighted by the results presented up to this point. Hereafter we shall concentrate our analysis up to $St = 0.5$, in the range where our methodology has been shown to provide accurate sound predictions.

6. Spectral proper orthogonal decomposition

(a) Equations

The Proper Orthogonal Decomposition seeks a set of linear independent functions constituting a basis that best represents a given dataset in terms of fluctuation energy [87,88]. For a turbulent flow, the POD functions are found through the maximization of the mean-square projection on the velocity field, which is performed via the integral Fredholm equation, as shown by Lumley [87]

$$\int S_{\hat{u}\hat{u}}(x_1, x_2) u_\omega(x_2) \mathrm{d}x_2 = \sigma u_\omega(x_1). \tag{6.1}$$

In the case of SPOD, the kernel $S_{\hat{u}\hat{u}}$ is the cross-spectral density matrix of the field of interest, which is Hermitian by construction. The Fredholm equation can then be recast as an equivalent eigenvalue decomposition:

$$S_{\hat{u}\hat{u}} = U\Sigma U^{-1}. \tag{6.2}$$

Since $S_{\hat{u}\hat{u}}$ is Hermitian, U is a unitary matrix, so that $U^H U = I$ and $U^H = U^{-1}$. The eigenmode decomposition may then be rewritten as,

$$S_{\hat{u}\hat{u}} = U\Sigma U^H, \tag{6.3}$$

which corresponds to the singular value decomposition of $S_{\hat{u}\hat{u}}$.

Since the eigenvectors are orthogonal to each other, it is possible to construct a rank-N representation of the CSD as

$$\widetilde{S}_{\hat{u}\hat{u}} = \sum_{k=1}^{N} u_k \sigma_k u_k^H, \tag{6.4}$$

where σ_k are the eigenvalues and u_k the eigenvectors of $S_{\hat{u}\hat{u}}$.
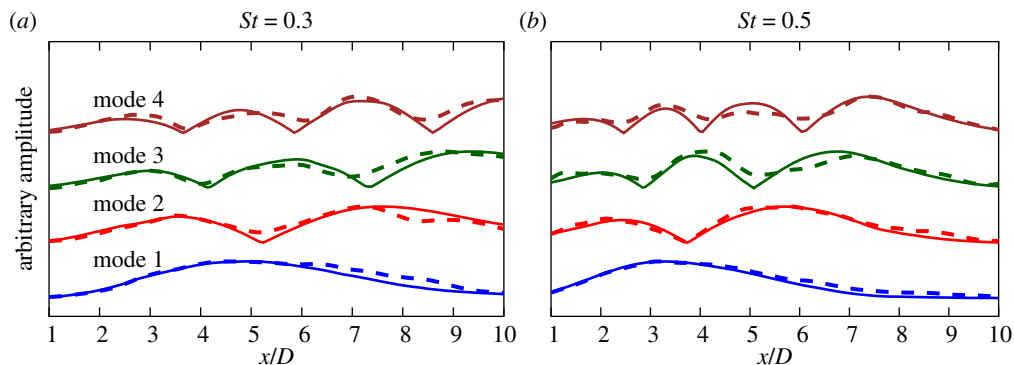
Figure 11. Structure of first four SPOD modes. Solid line represents the modes of the model CSD and dashed lines the modes of the CSD issued from the LES. The amplitudes are arbitrary and are in linear scale. (Online version in colour.)

The elements of the rank-N representation of the CSD are given as,

$$\left[\widetilde{S}_{\hat{u}\hat{u}}\right]_{x_1,x_2} = \sum_{k=1}^{N} u_k(x_1)\sigma_k u_k^H(x_2). \tag{6.5}$$

The rank-N representation of the coherence function is given as the rank-N CSD normalized by the rank-N PSD's at each of the points

$$\widetilde{\gamma}^2(x_1, x_2) = \frac{\left|\sum_{k=1}^{N} u_k(x_1)\sigma_k u_k^H(x_2)\right|^2}{\left[\sum_{k=1}^{N} u_k(x_1)\sigma_k u_k^H(x_1)\right]\left[\sum_{k=1}^{N} u_k(x_2)\sigma_k u_k^H(x_2)\right]}. \tag{6.6}$$

We can obtain the rank-1 coherence as,

$$\widetilde{\gamma}^2(x_1, x_2) = \frac{\left|u_1(x_1)\sigma_1 u_1^H(x_2)\right|^2}{\left[u_1(x_1)\sigma_1 u_1^H(x_1)\right]\left[u_1(x_2)\sigma_1 u_1^H(x_2)\right]} = \frac{|u_1(x_1)|^2 \, \sigma_1^2 \, |u_1(x_2)|^2}{|u_1(x_1)|^2 \, \sigma_1^2 \, |u_1(x_2)|^2} = 1, \tag{6.7}$$

showing that any single-mode representation of the CSD leads to unit coherence. In order to obtain two-point coherences lower than one, a superposition of $N > 1$ modes is necessary.

The far-field radiation of a rank-N CSD may be assessed via equation (2.21) by substituting the source term with the low-order representation,

$$\langle \tilde{p}(R,\theta,\omega)\tilde{p}^*(R,\theta,\omega)\rangle = \frac{k_a^4 \cos^4 \theta}{4R^2} \iint \left[\widetilde{S}_{\hat{u}\hat{u}}\right]_{x_1,x_2} e^{ik_a \cos\theta(x_1-x_2)} \, dx_1 dx_2. \tag{6.8}$$

(b) Envelopes and phases

SPOD was performed on the CSD issuing from both the LES data and the model. For the sake of compactness, throughout the remainder of the paper, we shall concentrate on results of the SPOD carried out at $St = 0.3$ and $St = 0.5$. However, results for $St = 0.4$ have similar behaviour for all the plots in this and in the subsequent sections. Figure 11 shows the amplitude envelopes of the first four modes. The amplitudes have been normalized in order to allow qualitative comparisons between the modes of the two CSD's. The first mode is a typical wavepacket with a nearly Gaussian envelope and subsequent modes have envelopes with a successively larger number of lobes; for instance, kth mode has k lobes and $k - 1$ minima points; this reflects the orthogonality of the basis that is formed by the modes. The spatial structure of the modes of the model CSD is in good agreement with those of the CSD issuing from the LES, especially for the first three modes. As the order of the model is increased, the tendency is that the agreement deteriorates, because a higher spatial resolution is required for the modes to be statistically converged [89].

The phases of the modes are shown in figure 12. The phase of the first mode displays a typical convective behaviour characterized by a straight line. The higher-order modes have π
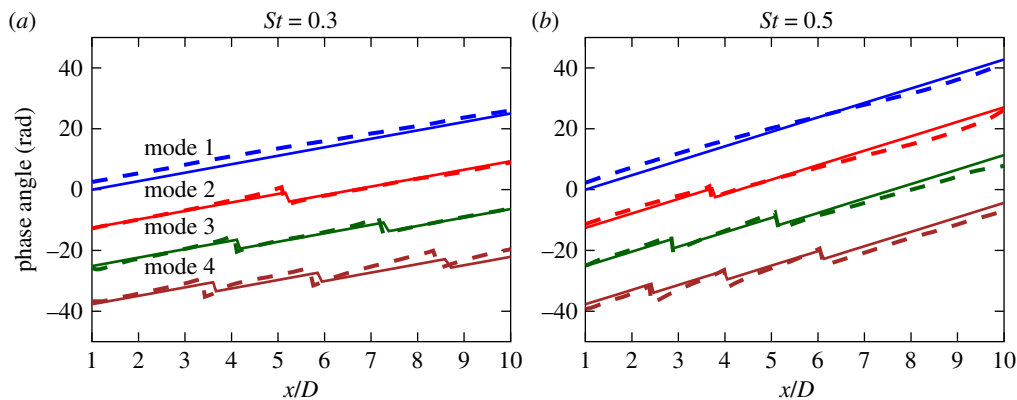
Figure 12. Phase of first four SPOD modes. Solid line represents the phases of the model CSD and dashed lines the phases of the CSD issued from LES data. (Online version in colour.)

phase jumps at axial positions corresponding to the minima positions of the envelopes; these characteristics stem from the orthogonality of the basis formed by the eigenfunctions. While they cannot be directly related to any specific flow structures, one can interpret the higher-order SPOD modes and their features as directions necessary to describe flow structures with more complex, jittery behaviour; therefore, they play a role in coherence decay by introducing a phase 'blur' between different axial stations. The phases of the modes of LES data also contain similar phase jumps.

Furthermore, we can see from figure 11 that there is a certain characteristic lengthscale that can be associated with each mode by taking the distance between successive lobes; this lengthscale decreases with increasing mode number, suggesting that higher-order modes are associated with smaller scale activity.

As discussed in the introduction, the link between SPOD modes and resolvent modes has been explored by other studies [73–75], and the results indicate high correlations between leading SPOD and resolvent modes, suggesting that coherence decay is underpinned by a rather disorganized, uncorrelated background turbulence forcing the linearized equations of motion and that the SPOD modes are structures that arise in response to this forcing and whose organization is imposed by the linear operator. The envelopes and phases of the modes shown in figures 11 and 12 suggest that background forcing leads to the multi-lobed structure and phase jumps manifest in the SPOD modes, which describe acoustically important degrees of wavepacket freedom and that cannot be captured using a standard linear stability analysis that neglects the forcing due to nonlinearities. We now address the question of the rank necessary to describe these acoustically important dynamics, by computing sound fields using truncated CSD source models, and by evaluating the effect of truncation both on the radiated sound and the source parameters that underpin this.

(c) Energy convergence

The convergence of the SPOD regarding the energy of the modes may be evaluated through

$$\frac{\sum_{i=1}^{k} \sigma_i}{\sum_{i=1}^{N} \sigma_i}, \tag{6.9}$$

where the sum of the energy captured by the first k eigenvalues is normalized by the sum of the total energy. Figure 13 shows the energy convergence for the model CSD for $0.3 \leq St \leq 0.5$. Between 10 and 20 modes are required to recover the energy of the full CSD, and it can be observed that the number of modes required to capture all of the energy contained in the CSD decreases as the Strouhal number is increased. This might lead to the conclusion that a low-rank
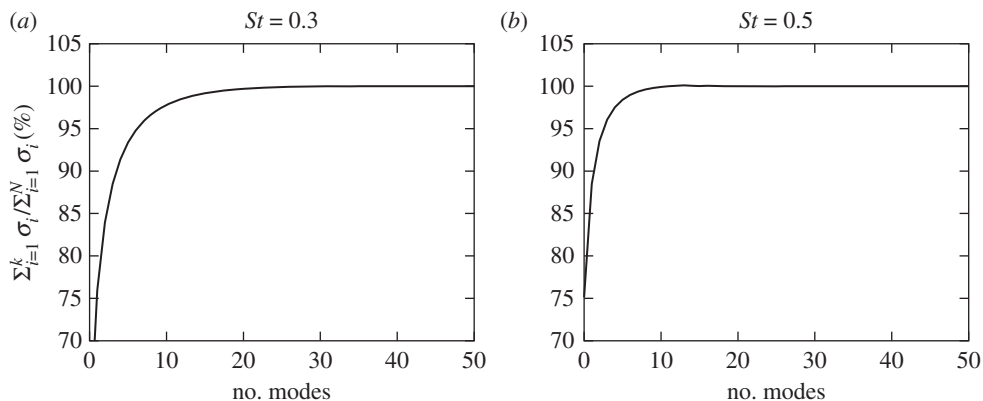
Figure 13. Cumulative energy of the first k eigenvalues normalized by the sum of the N computed eigenvalues.
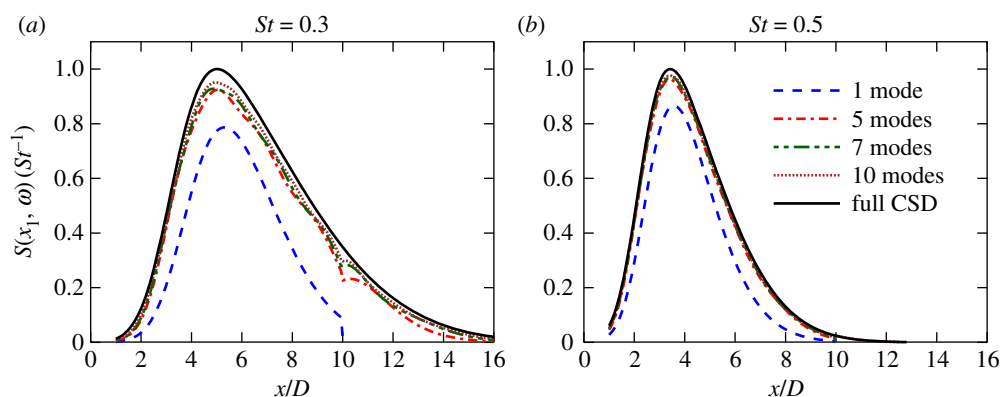

Figure 14. Wavepacket envelope convergence of different low-rank approximations. The levels have been normalized by the maximum value of the full source. (Online version in colour.)

behaviour only becomes pronounced with increasing Strouhal number. However, as can be seen in figure 9, most of the energy of the source lies outside the radiating region in wavenumber space, so that the number of modes required to recover the energy is not necessarily the same to capture the important acoustic features of the CSD. Thus, in the next section, we analyse the low-rank behaviour of the model regarding its acoustic radiation.

(d) Low-rank models

We assess the convergence of low-rank approximations of the CSD of the kinematic source model with respect to acoustic radiation, and to two sound source parameters considered earlier: amplitude envelope and coherence decay, which are not correctly captured by linear stability models.

Figure 14 shows the convergence of the envelopes of low-rank models with increasing numbers of modes with respect to the full CSD. We see that a one-mode representation underestimates the peak amplitude by approximately 20%; nevertheless, we note that the low-rank models quickly converge to the amplitude envelope of the full CSD. Only 7–10 modes in the reduced-order model suffice to capture the envelope length and amplitude.

As shown in equation (6.7), a low-rank representation of the CSD with only one mode results in unit coherence and so a higher-rank model is essential for this aspect of the wavepacket source behaviour. This is illustrated in figure 15, which shows the coherence envelopes of low-rank approximations with up to 10 modes, with reference point at the centre of the wavepacket, x_0.
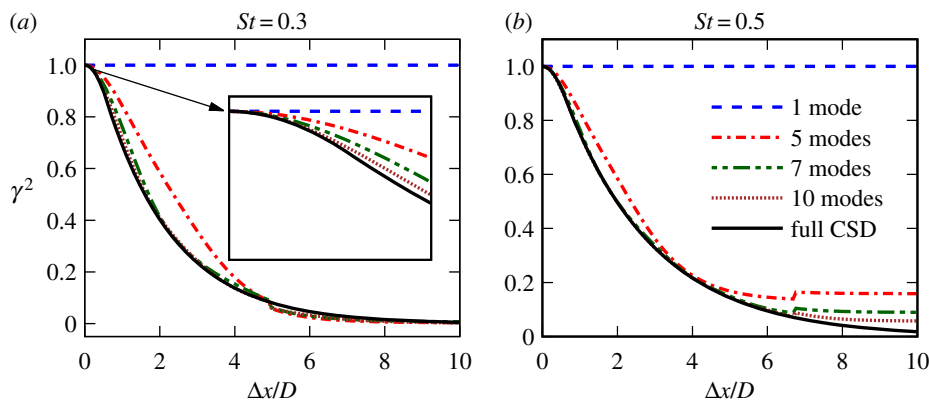
Figure 15. Coherence convergence of different low-rank approximations. Reference point is at x_0. (Online version in colour.)
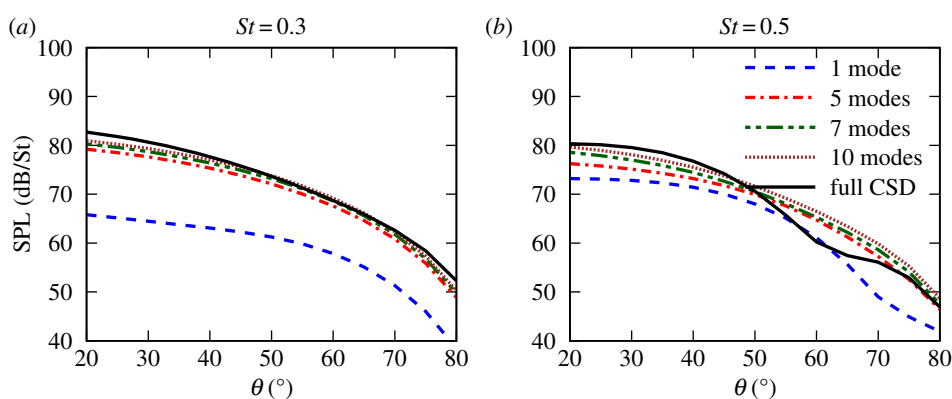

Figure 16. Effect of cumulative SPOD modes on far-field radiation by the wavepacket source. (Online version in colour.)

By successively adding more modes, the coherence decays more sharply and approaches the envelope of the full CSD.

The SPL of a low-rank approximation can be computed using equation (6.8). We note that the number of modes needed to recover the acoustic radiation of the full CSD increases with increasing Strouhal number. Nevertheless, for the Strouhal numbers considered, a low-rank representation of the source with 10 modes was sufficient to recover the acoustic efficiency of the full source model at low polar angles, as seen in figure 16. Due to its unit coherence, a low-rank model with only one mode has a very low acoustic efficiency, similar to the single-point wavepacket, as one can see by comparing figures 8 and 16.

Ten modes is less than the number of modes necessary to recover all of the energy contained in the CSD (figure 13) at lower Strouhal numbers ($St \leq 0.3$). This suggests that, at these Strouhal numbers, part of the energy is redundant from an acoustic point of view, and the correct representation of the wavepacket parameters is more relevant to sound radiation. These results reveal that this model source, which has been shown to produce the correct sound field at low polar angles, is relatively low-rank; wavepacket traits relevant to sound radiation, namely, coherence decay and envelope characteristic lengths, can be recovered with only a few SPOD modes.

7. Conclusion

The kinematic-sound source model proposed by Cavalieri & Agarwal [48] based on two-point statistics has been studied in order to get further insight into wavepacket parameters important

to sound radiation. Data from a large-eddy simulation performed using the flow solver 'Charles' [85] were used to educe the physical parameters necessary to compute the sound radiation by the model source, namely: the wavepacket characteristic lengthscales, L and L_{as}, the position where the envelope reaches its maximum, x_0, the envelope decay rate parameter, α, the hydrodynamic wavenumber, k_h and the coherence length scales, $L_{c_{1,2}}$.

Unlike past studies based on a line-source approach [44,51,58,80], we choose to take account of the radial structure of the source. And unlike Cavalieri *et al.* [44], we educe the source parameters directly from the two-point velocity measurements instead of estimating single-point parameters from the sound field, following the approach of previous studies [11,12,21–24]. The single-point model does not account for coherence decay, and thus the single-point parameters inferred from the acoustic field do not correspond to those educed from flow data, as shown in table 2. Due to the lack of coherence modulation in the single-point formulation, the correct source parameters can be considered to have been hidden in, or compensated for by, those inferred from the sound field; this highlights the caution that is necessary when using inverse approaches, as different source fields can lead to quite similar acoustic radiation. Using the parameters educed from LES data to animate the model, it was possible to compute the acoustic field through equation (2.21).

The results reveal the key importance of both coherence decay and envelope shape for wavepacket sound radiation. They show that, if coherence decay is neglected, most of the energy of the model source lies outside of the region of the spectrum corresponding to acoustically matched wavenumbers, and thus the single-point wavepacket has a very low acoustic efficiency. These results highlight the importance of coherence decay, the frequency domain manifestation of jitter, for jet noise modelling, which has been evoked in previous studies [41,47,51,52].

Furthermore, it has been shown that the asymmetry of the wavepacket envelope is also of key importance for an accurate sound prediction. An asymmetric envelope, which better represents flow data, produces sound levels closer to experimental results at low polar angles, especially at low Strouhal numbers. For $St > 0.5$ the model overpredicts the data due to the acoustic compactness assumption, which amounts to neglecting the radial structure of the Bessel function, $J_0(k_a r \sin \theta)$, in the far-field radiation equation.

We have used full-field data to characterize the three-dimensional structure of the CSD matrix, which is at the core of Lighthill's acoustic analogy. These data can be obtained for instance, through a high-fidelity simulation with converged two-point statistics, as the one we use; or alternatively, it can be obtained from an experiment involving simultaneous measurements in two-different flow planes, as the one carried out by Jaunet *et al.* [19]. In the absence of full-field data, simplifying assumptions about the structure of the CSD matrix have to be done, which can lead to the use of empirical constants to calibrate the source, as done in many studies in the past. However, the results have shown that a simplified wavepacket model relying on a relatively small number of parameters provides a fairly accurate sound prediction of the axisymmetric pressure mode at low polar angles. These observations give insight regarding perspectives for dynamic wavepacket models to predict jet noise without the need for such an extensive database: although the standard, unforced linear models successfully capture the phase speed and the amplitude envelope up to the point where the Kelvin–Helmholtz mode becomes stable [35,40,41], they underpredict the amplitude further downstream and do not contain information regarding coherence decay, making an accurate noise prediction impossible; on the other hand, other studies have shown that these issues may be overcome by using a forcing term in the linearized equations [90]. This and the fact that forced linear stability models can determine the amplitude of the fluctuations make them more suitable to describe sound generation mechanisms.

A Spectral Proper Orthogonal Decomposition of the model CSD was performed with a view to exploring the possibility of constructing a reduced-rank source model capable of capturing the acoustically important parameters. This is further motivated by the recently demonstrated link between SPOD modes and optimal resolvent response modes that arise when the linear stability models are considered in the presence of stochastic forcing [75].

An analysis of eigenvalue convergence reveals that approximately 10 to 20 modes are necessary to capture the total energy of the CSD, the number of modes decreasing with increasing

Strouhal number. On the other hand, only 10 modes are necessary to recover the most important traits for sound radiation, namely the envelope shape and coherence envelopes. This reveals that the acoustically important features can be reproduced with a low-rank model.

References

1. Lighthill MJ. 1952 On sound generated aerodynamically I. General theory. *Proc. R. Soc. Lond. A* **211**, 564–587. (doi:10.1098/rspa.1952.0060)
2. Lilley GM. 1974 On the noise from jets. In *AGARD Conf. Proc.*, number 131.
3. Goldstein ME. 2010 A generalized acoustic analogy. *J. Fluid Mech.* **488**, 315–333. (doi:10.1017/S0022112003004890)
4. Crow SC. 1970 Aerodynamic sound emission as a singular perturbation problem. *Stud. Appl. Math.* **49**, 21–46. (doi:10.1002/sapm197049121)
5. Freund JB. 2003 Noise-source turbulence statistics and the noise from a mach 0.9 jet. *Phys. Fluids* **15**, 1788. (doi:10.1063/1.1569919)
6. Colonius T, Freund JB. 2000 Application of Lighthill's equation to a mach 1.92 turbulent jet. *AIAA J.* **38**, 368–370. (doi:10.2514/2.966)
7. Davies POAL, Fisher MJ, Barrat MJ. 1963 The characteristics of turbulence in the mixing region of a round jet. *J. Fluid Mech.* **15**, 337–367. (doi:10.1017/S0022112063000306)
8. Bradshaw P, Ferris DH, Johnson RF. 1964 Turbulence in the noise-producing region of a circular jet. *J. Fluid Mech.* **19**, 591–624. (doi:10.1017/S0022112064000945)
9. Davies POAL. 1966 Turbulence structure in free-shear layers. *AIAA J.* **4**, 1971–1978. (doi:10.2514/3.3827)
10. Chu WT. 1966 *Turbulence measurements relevant to jet noise*. Technical Report 19, UTIAS, University of Toronto, Toronto, Canada, November.
11. Harper-Bourne M. 1999 Jet near-field noise prediction. In *Proc. 5th AIAA/CEAS Aeroacoustics Conf. Exhibit, Belleville, WA, 10–12 May*, number 1838. Reston, VA: AIAA.
12. Harper-Bourne M. 2003 Jet noise turbulence measurements. In *Proc. 9th AIAA/CEAS Aeroacoustics Conf. Exhibit, Hilton Head, SC, 12–14 May*, number 3214. Reston, VA: AIAA.
13. Morris PJ, Zaman KBMQ. 2010 Velocity measurements in jets with application to noise source modelling. *J. Sound Vib.* **239**, 394–414. (doi:10.1016/j.jsv.2009.09.024)
14. Jordan P, Gervais Y. 2005 Modelling self- and shear-noise mechanisms in inhomogeneous, anisotropic turbulence. *J. Sound Vib.* **279**, 529–555. (doi:10.1016/j.jsv.2003.11.045)
15. Kerhervé F, Fitzpatrick J, Jordan P. 2006 The frequency dependency of jet turbulence for noise source modelling. *J. Sound Vib.* **296**, 209–225. (doi:10.1016/j.jsv.2006.02.012)
16. Ukeiley L, Tinney C, Mann R, Glauser M. 2007 Spatial correlations in a transonic jet. *AIAA J.* **45**, 1357–1369. (doi:10.2514/1.26071)
17. Seiner JM, Ukeiley L, Ponton MK. 1999 Jet noise source measurements using piv. In *Proc. 5th AIAA/CEAS Aeroacoustics Conf. Exhibit, Belleville, WA, 10–12 May*, number 1869. Reston, VA: AIAA.

18. Bridges J, Wernet M. 2004 Measurements of the aeroacoustic sound source in hot jets. In *Proc. 10th AIAA/CEAS Aeroacoustics Conf. and Exhibit*, *Manchester, UK, 10–12 May*, number 212508. Reston, VA: AIAA.

19. Jaunet V, Jordan P, Cavalieri AVG. 2017 Two-point coherence of wavepackets in turbulent jets. *Phys. Rev. Fluids* **2**, 024604. (doi:10.1103/PhysRevFluids.2.024604)

20. Karabasov SA, Afsar MZ, Hynes TP, Dowling AP, MacMullan WA, Pokora CD, Page GJ, McGuirk JJ. 2010 Jet noise: acoustic analogy informed by large eddy simulation. *AIAA J.* **48**, 1312–1325. (doi:10.2514/1.44689)

21. Self RH. 2004 Jet noise prediction using Lighthill acoustic analogy. *J. Sound Vib.* **275**, 757–768. (doi:10.1016/j.jsv.2003.06.020)

22. Goldstein ME, Kharavan A. 2005 Acoustic source modelling for high speed air jets. In *Proc. 43rd Aerospace Sciences Meeting and Exhibit*, *Reno, NV, 10–13 January*, vol. 213416.

23. Goldstein ME, Leib SJ. 2008 The aeroacoustics of slowly diverging supersonic jets. *J. Fluid Mech.* **600**, 291–337. (doi:10.1017/S0022112008000311)

24. Leib SJ, Goldstein ME. 2011 Hybrid source model for predicting high-speed jet noise. *AIAA J.* **49**, 1324–1335. (doi:10.2514/1.J050707)

25. Tam CKW, Auriault L. 1999 Jet mixing noise from fine-scale turbulence. *AIAA J.* **37**, 145–153. (doi:10.2514/2.691)

26. Kharavan A, Krejsa EAZ, Kim CM. 1994 Computation of supersonic jet mixing noise for an axisymmetric convergent-divergent nozzle. *J. Aircraft* **31**, 603–609. (doi:10.2514/3.46537)

27. Mollo-Christensen E. 1963 *Measurements of near field pressure of subsonic jets*. Technical Report, DTCI.

28. Mollo-Christensen E. 1967 Jet noise and shear flow instability seen from an experimenter's viewpoint. *J. Appl. Mech.* **34**, 1–7. (doi:10.1115/1.3607624)

29. Crow S, Champagne F. 1971 Orderly structure in jet turbulence. *J. Fluid Mech.* **48**, 547–591. (doi:10.1017/S0022112071001745)

30. Cavalieri AVG, Jordan P, Lesshafft L. 2019 Wave-packet models for jet dynamics and sound radiation. *Appl. Mech. Rev.* **71**, 020802. (doi:10.1115/1.4042736)

31. Michalke A. 1970 *A wave model for sound generation from circular jets*. Technical Report, Deutsche Luft- und Raumfart.

32. Michalke A. 1972 An expansion scheme for the noise from circular jets. *Zeitschrift für Flugwissenschaften* **20**, 229–237.

33. Crighton DG, Gaster M. 1976 Stability of slowly diverging jet flow. *J. Fluid Mech.* **77**, 397–413. (doi:10.1017/S0022112076002176)

34. Jordan P, Colonius T. 2013 Wave packets and turbulent jet noise. *Annu. Rev. Fluid Mech.* **45**, 173–195. (doi:10.1146/annurev-fluid-011212-140756)

35. Cavalieri AVG, Rodríguez D, Jordan P, Colonius T, Gervais Y. 2013 Wavepackets in the velocity field of turbulent jets. *J. Fluid Mech.* **730**, 559–592. (doi:10.1017/jfm.2013.346)

36. Kerhervé F, Jordan P, Cavalieri AVG, Delville J, Bogey C, Juvé D. 2012 Educing the source mechanism associated with downstream radiation in subsonic jets. *J. Fluid Mech.* **710**, 606–640. (doi:10.1017/jfm.2012.378)

37. Rodríguez D, Cavalieri AVG, Colonius T, Jordan P. 2015 A study of wavepacket models for subsonic turbulent jets using local eigenmode decomposition of piv data. *Eur. J. Mech. B/Fluids* **49**, 308–321. (doi:10.1016/j.euromechflu.2014.03.004)

38. Tinney CE, Jordan P. 2008 The near pressure field of co-axial subsonic jets. *J. Fluid Mech.* **611**, 175–204. (doi:10.1017/S0022112008001833)

39. Suzuki T, Colonius T. 2006 Instability waves in a subsonic round jet detected using a near-field phased microphone array. *J. Fluid Mech.* **565**, 197–226. (doi:10.1017/S0022112006001613)

40. Gudmundsson K, Colonius T. 2011 Instability wave models for the near-field fluctuations of turbulent jets. *J. Fluid Mech.* **689**, 97–128. (doi:10.1017/jfm.2011.401)

41. Breakey DES, Jordan P, Cavalieri AVG, Nogueira PA, Léon O, Colonius T, Rodríguez D. 2017 Experimental study of turbulent-jet wave packets and their acoustic efficiency. *Phys. Rev. Fluids* **2**, 124601. (doi:10.1103/PhysRevFluids.2.124601)

42. Crow SC. 1972 Acoustic gain of a turbulent jet. In *Paper IE.6, Meeting of Division of Fluid Dynamics*, *American Physical Society*. Boulder, CO: University of Colorado.

43. Michalke A, Fuchs HV. 1975 On turbulence and noise of an axisymmetric shear flow. *J. Fluid Mech.* **70**, 179–205. (doi:10.1017/S0022112075001966)

44. Cavalieri AVG, Jordan P, Colonius T, Gervais Y. 2012 Axisymmetric superdirectivity in subsonic jets. *J. Fluid Mech.* **704**, 388–420. (doi:10.1017/jfm.2012.247)

45. Kopiev V, Chernyshev S, Faranosov G, Zaitsev M, Belyaev I. 2010 Correlations of jet noise azimuthal components and their role in source identification. In *16th AIAA/CEAS Aeroacoustics Conf.* Stockholm, Sweden: AIAA.

46. Brès GA, Jordan P, Jaunet V, Le-Rallic M, Cavalieri AVG, Towne A, Lele SK, Colonius T, Schmidt OT. 2018 Importance of the nozzle-exit boundary-layer state in subsonic turbulent jets. *J. Fluid Mech.* **851**, 83–124. (doi:10.1017/jfm.2018.476)

47. Baqui YB, Agarwal A, Cavalieri AVG, Sinayoko S. 2015 A coherence-matched linear mechanism for subsonic jets. *J. Fluid Mech.* **776**, 235–267. (doi:10.1017/jfm.2015.322)

48. Cavalieri AVG, Agarwal A. 2014 Coherence decay and its impact on sound radiation by wavepackets. *J. Fluid Mech.* **748**, 399–415. (doi:10.1017/jfm.2014.186)

49. Jordan P, Colonius T, Brès GA, Zhang M, Towne A, Lele S. 2014 Modelling intermittent wavepackets and their radiated sound in a turbulent jet. In *Summer Program*. Stanford, CA: Center for Turbulent Research.

50. Zhang M, Jordan P, Lehnasch G, Cavalieri AVG, Agarwal A. 2014 Just enough jittering for jet noise. In *Proc. 20th AIAA/CEAS Aeroacoustics Conf. Exhibit*, *Atlanta, GA, 16–20 June*. Reston, VA: AIAA.

51. Cavalieri AVG, Jordan P, Agarwal A, Gervais Y. 2011 Jittering wave-packet models for subsonic jet noise. *J. Sound Vib.* **330**, 4474–4492. (doi:10.1016/j.jsv.2011.04.007)

52. Ffwocs-Williams JE, Kempton AJ. 1978 The noise from the large-scale structure of a jet. *J. Fluid Mech.* **84**, 673–694. (doi:10.1017/S0022112078000415)

53. Crighton DG. 1975 Basic principles of aerodynamic noise generation. *Prog. Aerosp. Sci.* **16**, 31–96. (doi:10.1016/0376-0421(75)90010-X)

54. Crighton DG, Huerre P. 1990 Shear-layer pressure fluctuations and superdirective acoustic sources. *J. Fluid Mech.* **220**, 355–368. (doi:10.1017/S0022112090003299)

55. Cavalieri AVG, Jordan P, Wolf WR, Gervais Y. 2014 Scattering of wavepackets by a flat plate in the vicinity of a turbulent jet. *J. Sound Vib.* **333**, 6516–6531. (doi:10.1016/j.jsv.2014.07.029)

56. Piantanida S, Jaunet V, Huber J, Wolf WR, Jordan P, Cavalieri AVG. 2016 Scattering of turbulent-jet wavepackets by a swept trailing edge. *J. Acoust. Soc. Am.* **140**, 4350–4359. (doi:10.1121/1.4971425)

57. Nogueira PAS, Cavalieri AVG, Jordan P. 2016 A model problem for sound radiation by and installed jet. In *Proc. 22th AIAA/CEAS Aeroacoustics Conf. and Exhibit*, *Lyon, France, 30 May–1 June*. Reston, VA: AIAA.

58. da-Silva FD, Deschamps CJ, Jordan P, Piantanida S, Cavalieri AVG, Brès G. 2016 Effects of coherence on jet-surface interaction noise. In *Proc. 22th AIAA/CEAS Aeroacoustics Conf. Exhibit*, *Lyon, France, 30 May–1 June*. Reston, VA: AIAA.

59. Michalke A. 1983 Some remarks on source coherence affecting jet noise. *J. Sound Vib.* **87**, 1–17. (doi:10.1016/0022-460X(83)90436-4)

60. Reba R, Narayanan S, Colonius T, Suzuki T. 2005 Modeling jet noise from organized structures using near-field hydrodynamic pressure. In *Proc. 11th AIAA/CEAS Aeroacoustics Conf. Exhibit*, *Monterey, CA, 23–25 May*, number 3093. Reston, VA: AIAA.

61. Reba R, Simonich J, Schlinker R. 2008 Measurements of source wave-packets in high-speed jets and connection to far-field sound. In *Proc. 14th AIAA/CEAS Aeroacoustics Conf. Exhibit*, *Vancouver, BC, 5–7 May*, number 3256. Reston, VA: AIAA.

62. Reba R, Simonich J, Schlinker R. 2009 Sound radiated by large-scale wave-packets in subsonic and supersonic jets. In *Proc. 15th AIAA/CEAS Aeroacoustics Conf. Exhibit*, *Miami, FL, 11–13 May*, number 3256. Reston, VA: AIAA.

63. Reba R, Narayanan S, Colonius T. 2010 Wave-packet models for large-scale mixing noise. *Int. J. Aeroacoustics* **9**, 533–558. (doi:10.1260/1475-472X.9.4-5.533)

64. Brès G, Ham FE, Nichols JW, Lele SK. 2017 Unstructured large-eddy simulations of supersonic jets. *AIAA J.* **55**, 1164–1184. (doi:10.2514/1.J055084)

65. Kopiev VF, Chernyshev SA. 2014 Simulation of azimuthal characteristics of turbulent jet noise by correlation model of quadrupole sources. *Int. J. Aeroacoustics* **13**, 39–60. (doi:10.1260/1475-472X.13.1-2.39)

66. Kopiev VF, Chernyshev SA. 2015 Refraction effect in correlation model of quadrupole noise sources in turbulent jet. In *Proc. 21st AIAA/CEAS Aeroacoustics Conf. Exhibit*, *Dallas, TX, 22–26 June*. Reston, VA: AIAA.

67. Kopiev VF, Chernyshev SA. 2012 Correlation model for noise sources in turbulent jet based on birth of vortices as a key event. In *Proc. 18th AIAA/CEAS Aeroacoustics Conf. Exhibit*, *Colorado Springs, CO, 4–6 June*. Reston, VA: AIAA.

68. Farell BF, Ioannou P. 2001 Accurate low-dimensional approximation of the linear dynamics of fluid flow. *J. Atmos. Sci.* **58**, 2771–2789. (doi:10.1175/1520-0469(2001)058<2771:ALDAOT>2.0.CO;2)

69. Hwang Y, Cossu C. 2010 Linear non-normal energy amplification of harmonic and stochastic forcing in the turbulent channel flow. *J. Fluid Mech.* **654**, 51–73. (doi:10.1017/S0022112010003629)

70. Bagheri S, Henningson DS, Hoepffner J, Schmid PJ. 2009 Input-output analysis and control design applied to a linear model of spatially developing flows. *Appl. Mech. Rev.* **62**, 020803. (doi:10.1115/1.3077635)

71. McKeon BJ, Sharma AS. 2010 A critical-layer framework for turbulent pipe flow. *J. Fluid Mech.* **658**, 336–382. (doi:10.1017/S002211201000176X)

72. Tissot G, Zhang M, Laús-Jr FC, Cavalieri AVG, Jordan P. 2017 Sensitivity of wavepackets in jets to nonlinear effects: the role of the critical layer. *J. Fluid Mech.* **811**, 95–137. (doi:10.1017/jfm.2016.735)

73. Semeraro O, Jaunet V, Jordan P, Cavalieri AVG, Lesshafft L. 2016 Stochastic and harmonic optimal forcing in subsonic jets. In *Proc. 22nd AIAA/CEAS Aeroacoustics Conf. Exhibit*, *Lyon, France, 30 May–1 June*. Reston, VA: AIAA.

74. Towne A, Colonius T, Jordan P, Cavalieri AVG, Brès G. 2015 Stochastic and nonlinear forcing of wavepackets in a mach 0.9 jet. In *Proc. 21st AIAA/CEAS Aeroacoustics Conf. Exhibit*, *Dallas, TX, 22–26 June*. Reston, VA: AIAA.

75. Towne A, Schmidt OT, Colonius T. 2018 Spectral proper orthogonal decomposition and its relationship to dynamic mode decomposition and resolvent analysis. *J. Fluid Mech.* **847**, 821–867. (doi:10.1017/jfm.2018.283)

76. Suzuki T. 2013 Coherent noise sources of a subsonic round jet investigated using hydrodynamic and acoustic phased-micriphone arrays. *J. Fluid Mech.* **730**, 659–698. (doi:10.1017/jfm.2013.337)

77. Landahl MT, Mollo-Christensen E. 1992 *Turbulence and random processes in fluid mechanics*. Cambridge, UK: Cambridge University Press.

78. Bodony DJ, Lele SK. 2008 Low-frequency sound sources in high-speed turbulent jets. *J. Fluid Mech.* **617**, 231–253. (doi:10.1017/S0022112008004096)

79. Goldstein M. 1976 *Aeroacoustics*. New York, NY: McGraw-Hill.

80. Nogueira PAS, Cavalieri AVG, Jordan P. 2017 A model problem for sound radiation by an installed jet. *J. Sound Vib.* **391**, 95–115. (doi:10.1016/j.jsv.2016.12.015)

81. Jordan P, Wells R, Gervais Y, Delville J. 2004 Optimisation of correlation function models for statistica aeroacoustic noise prediction. In *CFA/DAGA Aeroacoustics Conf*.

82. O'Hara D, Andersson N, Jordan P, Bilsson M, Eriksson L, davidson L. 2004 A hybrid analysis methodology for improved accuracy in low cost jet noise modelling. In *33rd Int. Congress Exposition on Noise Control Engineering*, *San Francisco, CA*.

83. Papamouschou D. 2010 Prediction of jet noise shielding. In *Proc. 48th AIAA Aerospace Sciences Meeting, Orlando, FL, 4–7 January*. Reston, VA: AIAA.

84. Koenig M, Cavalieri AVG, Jordan P, Delville J, Gervais Y. 2013 Farfield filtering and source imaging of subsonic jet noise. *J. Sound Vib.* **332**, 4067–4088. (doi:10.1016/j.jsv.2013.02.040)

85. Schmidt OT, Towne A, Rigas G, Colonius T, Brès GA. 2018 Spectral analysis of jet turbulence. *J. Fluid Mech.* **855**, 953–982. (doi:10.1017/jfm.2018.675)

86. Kopiev VF, Chernyshev SA. 2012 New correlation model for the cascade of turbulent pulsations as a noise source in turbulent jets. *Acoust. Phys.* **58**, 442–456. (doi:10.1134/S1063771012040112)

87. Lumley JL. 1967 The structure of inhomogeneous turbulent flows. *Atmospheric turbulence and radio wave propagation* (eds AM Yaglom, VI Tatarsky), pp. 168–178. Moscow, Russia: Nauka.

88. Citriniti JH, George WK. 2000 Reconstruction of the global velocity field in the axisymmetric mixing layer utilizing the proper orthogonal decomposition. *J. Fluid Mech.* **418**, 137–166. (doi:10.1017/S0022112000001087)

89. Jaunet V. 2017 Convergence of pod modes. Private communications.

90. Jordan P, Zhang M, Lehnasch G, Cavalieri AVG. 2017 Modal and non-modal linear wavepacket dynamics in turbulent jets. In *Proc. 23rd AIAA/CEAS Aeroacoustics Conference, Denver, CO, 5–9 June*. Reston, VA: AIAA.